



1 **Multidecadal ozone trends in China and implications for human**
2 **health and crop yields: A hybrid approach combining chemical**
3 **transport model and machine learning**

4 Jia Mao¹, Amos P. K. Tai^{1,2,3}, David H. Y. Yung¹, Tiangang Yuan¹, Kong T. Chau¹, and Zhaozhong
5 Feng^{2,4}

6 ¹ Earth and Environmental Sciences Programme and Graduate Division of Earth and Atmospheric Sciences, Faculty of
7 Science, The Chinese University of Hong Kong, Sha Tin, Hong Kong SAR, China

8 ² Collaborative Innovation Center on Forecast and Evaluation of Meteorological Disasters (CIC-FEMD), Nanjing
9 University of Information Science and Technology, Nanjing 210044, Jiangsu, China

10 ³ State Key Laboratory of Agrobiotechnology, and Institute of Environment, Energy and Sustainability, The Chinese
11 University of Hong Kong, Hong Kong SAR, China

12 ⁴ Key Laboratory of Ecosystem Carbon Source and Sink, China Meteorological Administration (ECSS-CMA), Nanjing
13 University of Information Science & Technology, Nanjing, 210044, China

14 *Correspondence to:* Amos P. K. Tai (amostai@cuhk.edu.hk)

15 **Abstract.** Surface ozone (O₃) is well known to pose significant threats to both human health and crop production worldwide.
16 However, a multi-decadal assessment of O₃ impacts on public health and crop yields in China is lacking due to insufficient
17 long-term continuous O₃ observations. In this study, we used a machine learning (ML) algorithm to correct the biases of
18 O₃ concentrations simulated by the chemical transport model from 1981–2019 by integrating multi-source datasets. The
19 ML-enabled bias correction offers improved performance in reproducing observed O₃ concentrations, and thus further
20 improves our estimates of O₃ impacts on human health and crop yields. Our results show that a warm-season increasing
21 trend of O₃ in Beijing-Tianjin-Hebei and its surroundings (BTHs), Yangtze River Delta (YRD), Sichuan Basin (SCB) and
22 Pearl River Delta (PRD) regions are 0.32 μg m⁻³ yr⁻¹, 0.63 μg m⁻³ yr⁻¹, 0.84 μg m⁻³ yr⁻¹, and 0.81 μg m⁻³ yr⁻¹ from 1981
23 to 2019, respectively. In more recent years, O₃ concentrations experience more fluctuations in the four major regions. Our
24 results show that only BTHs have a perceptible increasing trend of 0.81 μg m⁻³ yr⁻¹ during 2013–2019. Meteorological
25 factors play important roles in modulating the interannual variability of surface O₃, wherein synoptic systems (e.g., high-
26 pressure system, Western Pacific subtropical high, tropical cyclone) are closely related to the spatiotemporal distribution
27 of regional O₃ via influencing regional weather conditions and transport processes. Using AOT40-China dose-yield
28 relationship, the estimated relative yield losses (RYLs) for wheat, rice, soybean and maize are 17.6%, 13.8%, 11.3% and
29 7.3% in 1981, and increases to 24.2%, 17.5%, 16.3% and 9.8% in 2019, with an increasing rate of +0.03% yr⁻¹, +0.04%
30 yr⁻¹, +0.27% yr⁻¹ and +0.13% yr⁻¹, respectively. The estimated annual all-cause premature deaths induced by O₃ increase
31 from ~55,900 in 1981 to ~162,000 in 2019 with an increasing trend of ~2,980 deaths yr⁻¹. The annual premature deaths
32 related to respiratory and cardiovascular disease are ~34,200 and ~40,300 in 1998, and ~26,500 and ~79,000 in 2019,
33 having a rate of change of -546 and +1,770 deaths yr⁻¹ during 1998–2019, respectively. Our study, for the first time, used
34 ML to provide a robust dataset of O₃ concentrations over the past four decades in China, enabling a long-term evaluation
35 of O₃-induced crop losses and health impacts. These findings are expected to fill the gap of the long-term O₃ trend and
36 impact assessment in China.



37 1 Introduction

38 Surface ozone (O_3), an important secondary air pollutant, is mainly generated through photochemical reaction of
39 volatile organic compounds (VOCs), carbon monoxide (CO), and nitrogen oxides (NO_x) in the presence of sunlight. As a
40 strong oxidant, O_3 at the ground level is detrimental to human health and vegetation. More recently, due to the rapid
41 urbanization and industrialization, the summertime O_3 pollution has become an emerging concern in China. Li et al. (2020)
42 reported that the mean summer 2013–2019 trend in maximum daily 8-h average surface O_3 (MDA8- O_3) was $+1.9 \text{ ppb yr}^{-1}$
43 in China, with high values widely observed in the North China Plain (NCP), Yangtze River Delta (YRD), and Pearl River
44 Delta (PRD) regions. On the regional scale, the exposure of humans and vegetation to O_3 is greater in China than in other
45 developed regions of the world (Lu et al., 2018). Several studies have suggested the important roles of climate and land
46 cover changes on O_3 pollution in addition to anthropogenic emissions (Fu and Tai, 2015; Wang et al., 2020). It has been
47 suggested that global warming and the changing land use may further increase surface O_3 by the late 21st century (Kawase
48 et al., 2011; Wang et al., 2020), which can pose greater threats to human health and food security.

49 Meteorological factors can modulate the temporal and spatial patterns of O_3 via affecting the physical and chemical
50 processes within the atmosphere (Liu et al., 2019; Mao et al., 2020; Yin and Ma, 2020). High temperature, low relative
51 humidity and low planetary boundary height are conducive to the photochemical production and O_3 accumulation. Jacob
52 and Winner (2009) summarized that the enhanced O_3 levels at higher temperatures are primarily driven by increased
53 biogenic VOC emissions from vegetation and reduced lifetimes of peroxyacetyl nitrate (PAN) due to accelerated
54 decomposition of PAN into NO_x . Besides, the changes in wind speed and direction can affect O_3 concentrations through
55 transport. Land cover and land use change affects O_3 air quality by perturbing surface fluxes, hydrometeorology, and
56 concentrations of atmospheric chemical components (Tai et al., 2013; Fu and Tai, 2015; Liu et al., 2020; Ma et al., 2021).
57 For instance, the terrestrial biosphere is a major source of isoprene, which plays a significant role in modulating O_3
58 concentrations. In the Intergovernmental Panel on Climate Change (IPCC) A1B scenario, Tai et al. (2013) found that
59 widespread crop expansion could reduce isoprene emission by $\sim 10\%$ globally compared with the present land use. Such
60 a reduction could decrease O_3 by up to 4 ppb in the eastern US and increase O_3 by up to 6 ppb in South and Southeast Asia,
61 whereby the difference in the sign of responses is primarily determined by the different O_3 production regimes.

62 The increasing health burden due to air pollution has become an important contributor to global disease burden. Some
63 recent studies have demonstrated that short-term O_3 exposure negatively impacts human health, especially via respiratory,
64 and cardiovascular mortality (Shang et al., 2013; Yin et al., 2017b; Feng et al., 2019; Zhang et al., 2022a). In 2015–2018,
65 the estimated annual total premature mortality related to O_3 pollution in 334 Chinese cities was 0.27 million for 2015, 0.28
66 million for 2016, 0.39 million for 2017, and 0.32 million for 2018 (Zhang et al., 2021). Maji and Namdeo (2021) reported
67 that short-term all-cause, cardiovascular and respiratory premature mortalities attributed to the ambient 4th highest MDA8-
68 O_3 exposure were 156,000, 73,500 and 28,600 in 2019, showing increases of 19.6%, 19.8% and 21.2%, respectively,
69 compared to 2015. Zhang et al. (2022b) reported that each $10 \mu\text{g m}^{-3}$ increase in the MDA8- O_3 can lead to a rise of 0.41 %
70 (95 % CI: 0.35 %–0.48 %) in all-cause, 0.60 % (95 % CI: 0.51 %–0.68 %) in cardiovascular and 0.45 % (95 % CI: 0.28 %–
71 0.62 %) in respiratory mortality.

72 The damage to plants induced by O_3 is mainly caused by the stomatal uptake of O_3 into the leaf interior instead of
73 direct plant surface deposition (e.g., Clifton et al., 2020). In previous studies, a variety of concentration-based metrics have
74 been widely used to assess the O_3 risks to crop yield and ecosystem functions. Initially, a 7-hour (09:00–15:59) mean metric
75 (M7) was proposed, which was later extended to a 12-hour (08:00–19:59; referred to M12) to include late-day O_3
76 concentrations. Cumulative metrics have also been developed to evaluate the impacts of O_3 on crops. The accumulated O_3
77 over a threshold of 40 ppb (AOT40) is a widely used metric to evaluate the phytotoxic effects of O_3 . Compared to AOT40
78 using a linear function, another metrics, W126, considers the nonlinear response of yield loss to O_3 exposure whereby
79 higher O_3 concentrations will progressively induce more severe yield losses. However, many studies have suggested that
80 the stomatal uptake of O_3 is more related to vegetation damage than O_3 exposure per se (Feng et al., 2012; Feng et al., 2018;



81 Pleijel et al., 2022). In the recent two decades, the flux-based approach therefore has been developed and increasingly used
82 to assess the relationships between the stomatal O₃ uptake and crop yields. Tai et al. (2021) compared the results of the
83 estimated global crop yield losses using three concentration-based and two flux-based O₃ exposure metrics, and showed
84 that the concentration-based metrics differ greatly among themselves, while the two flux-based metrics are generally close
85 to each other, which lie close to the middle of the range covered by all metrics.

86 At present, a comprehensive long-term assessment of O₃ impacts is hindered by a lack of continuous O₃ observations
87 in China (Lu et al., 2018; Gong et al., 2021). From both health and food perspectives, reliable long-term estimates of O₃
88 are critically needed to better understand the O₃ damage over the past few decades since the beginning of rapid industrial
89 transformation in the 1980s. In previous studies, various alternative approaches have been used to address the problem of
90 insufficient observations. The multiple linear regression (MLR) model is often used for extrapolation to construct
91 spatiotemporal distributions of air pollutants (Moustris et al., 2012; Abdullah et al., 2017). However, the linear statistical
92 methods are generally limited by their incapability to capture the nonlinear relationships between air pollutants and
93 precursors as well as meteorological fields. Chemical transport models (CTMs), based on mathematical representation of
94 atmospheric physical and chemical processes, are also the common tool to simulate air pollutant concentrations
95 spatiotemporally (Fusco and Logan, 2003; Liu and Wang, 2020b; Wang et al., 2022a). Taking the advantages of the CTM,
96 Fu and Tai (2015) investigated the impacts of historical climate and land cover changes on tropospheric O₃ in East Asia
97 between 1980 and 2010. However, the utility of CTMs is often limited by their high computational cost when conducting
98 long-term simulations at high spatiotemporal resolutions. Large biases also exist due to uncertainties in historical emission
99 inventories, parameterization of physical and chemical processes, and initial and/or boundary conditions, and these errors
100 tend to increase at finer spatiotemporal scales.

101 In recent years, machine learning (ML) methods have gained increasing popularity in air pollution studies (Liu et al.,
102 2020; Ma et al., 2021). In the early stage of applying ML to atmospheric chemistry, ML methods were usually used as an
103 independent method from CTMs (Hu et al., 2017; Zhan et al., 2017), for instance, to predict O₃ concentrations by mapping
104 the nonlinear relationships between observed O₃ concentrations and their possible shaping factors. These applications are
105 usually purely data-driven, whereby the ML algorithms do not involve any representation of the physical mechanisms
106 behind the relevant processes. With powerful algorithms and user-friendly hyperparameter tuning processes, some well-
107 trained ML models, driven by data from multiple sources including reanalysis and satellite data, have shown even higher
108 predictive capacity than process-based models. The advantages of ML methods over CTMs include more flexible choices
109 for input data and spatiotemporal resolution, and substantially lower computational costs (Bi et al., 2022). However, purely
110 data-driven ML methods are known to suffer a lack of transparency and interpretability, which renders it more difficult to
111 offer adequate scientific interpretation for the physical mechanisms behind. Thus, a hybrid approach combining ML
112 algorithms and CTM-simulated results have been increasingly used to predict air pollutants and understand their trends in
113 recent years. Integrating data from various sources, ML methods have been used as a tool to correct the biases in the lower-
114 resolution simulated results from CTMs (Di et al., 2017; Ivatt and Evans, 2020; Ma et al., 2021). Based on process-based
115 CTMs integrating decades of accumulated knowledge in Earth system science, while taking advantage of ML to address
116 still-existing model errors, the hybrid approach has great potential in tackling air quality problems (Irrgang et al., 2021).

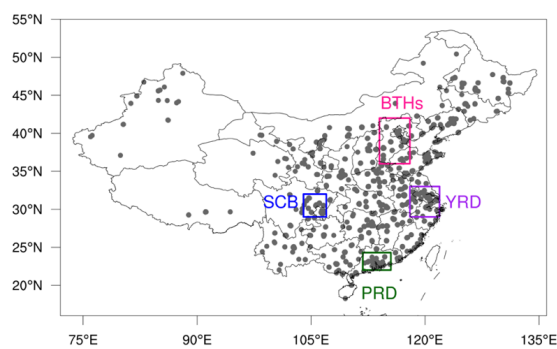
117 In this work, we incorporated the O₃ concentrations directly simulated by the Goddard Earth Observing System
118 coupled with Chemistry (GEOS-Chem) model at a lower resolution into a bias-corrected, finer-resolution dataset by
119 integrating them with O₃ observations from 2016 to 2018 (for validation purpose), high-resolution meteorological fields,
120 land use data and other geographical information from multiple sources using a tree-based ML algorithm, LightGBM. The
121 final high-resolution hourly O₃ dataset with a resolution of 0.25°×0.25° from 1981 to 2019 was further used to assess the
122 impacts of O₃ on human health and crop yields over the past four decades. The simultaneous analysis of the combined
123 impacts of O₃ on agriculture and human health can offer more comprehensive policy implications for the mitigation of O₃-
124 related impacts across China.



125 **2 Data and methods**

126 **2.1 Air quality, meteorological, land and crop data**

127 Hourly surface O₃ observations ($\mu\text{g m}^{-3}$) from 2016 to 2018 were obtained from the China National Environment
128 Monitoring Center Network (<http://106.37.208.233:20035/>) established by the Ministry of Ecology and Environment of
129 China. The MDA8-O₃ of each site was calculated with at least 14 valid hourly values from 08:00 to 24:00 local time. A
130 total of 1016 sites were selected after deleting the missing and abnormal data (**Fig. 1**).



131 **Figure 1. Study domain and locations of the selected monitoring sites. The pink, blue, purple and green rectangles**
132 **indicate the Beijing-Tianjin-Hebei and its surroundings (BTHs), Sichuan Basin (SCB), Yangtze River Delta (YRD),**
133 **and Pearl River Delta (PRD) regions, respectively, for more detailed analysis.**
134

135 The surface meteorological fields used in this study include sea surface pressure, horizontal wind at 10 m, air
136 temperature at 2 m, downward solar radiation, surface albedo, and total precipitation. The variables selected at 850 hPa
137 and 100 hPa include relative humidity, horizontal and vertical velocity. These meteorological variables have been shown
138 by many previous studies to correlate strongly with surface O₃ concentrations as discussed above. Hourly reanalysis data
139 for meteorological variables were obtained from the fifth generation European Center for Medium-Range Weather
140 Forecasts (ECMWF) reanalysis dataset (ERA5) with a spatial resolution of $0.25^\circ \times 0.25^\circ$ from 1981 to 2019
141 (<https://cds.climate.copernicus.eu/>). This spatial resolution sets the highest limit of resolution for our hybrid O₃ product.

142 The national land use data with a spatial resolution of $1 \text{ km} \times 1 \text{ km}$ for 2013 were obtained from the Resource and
143 Environment Science Data Center of the Chinese Academy of Sciences (RESDC) (<http://www.resdc.cn>). Six primary types
144 of land use are considered: cultivated land, forestland, grassland, water bodies, construction land, and unused land.
145 Nationwide elevation data were also provided by the RESDC (<https://www.resdc.cn/data.aspx?DATAID=123>), which is
146 resampled based on the latest Shuttle Radar Topography Mission (SRTM) V4.1 data developed in 2000.

147 The spatial distribution of the harvested areas for four staple crops (wheat, rice, maize, soybean) for China was
148 obtained from the Global Agro-Ecological Zones 2015 dataset (<https://doi.org/10.7910/DVN/KJFU01>). Crop harvesting
149 dates with a resolution of $0.5^\circ \times 0.5^\circ$ were provided by the Center for Sustainability and the Global Environment (Sacks et
150 al., 2010). For crops having more than one growing season in a year, only the primary growing period was considered.

151 **2.2 GEOS-Chem model**

152 We used the GEOS-Chem global 3-D chemical transport model version 12.2.0 (<http://acmg.seas.harvard.edu/geos/>),
153 driven by assimilated meteorological data from Modern Era Retrospective-analysis for Research and Applications, Version
154 2 (MERRA2) (<https://gmao.gsfc.nasa.gov/reanalysis/MERRA-2/>) with a horizontal resolution of 2.0° latitude by 2.5°



155 longitude and reduced vertical resolution of 47 levels. GEOS-Chem incorporates meteorological conditions, emissions,
156 chemical information, and surface conditions to simulate the formation, transport, mixing and deposition of ambient O₃. It
157 performs fully coupled simulations of O₃-NO_x-VOC-aerosol chemistry (Bey et al., 2001). Previous studies have
158 demonstrated the ability of GEOS-Chem to reasonably reproduce the magnitudes and seasonal variations of surface O₃
159 East Asia (Wang et al., 2011; He et al., 2012). To provide long-term simulated O₃ fields for incorporation into the ML
160 model (see below), we conducted GEOS-Chem simulations at a resolution of 2.0°×2.5°; higher resolutions of GEOS-Chem
161 in nested grids are available but computationally prohibitive for multi-decadal simulations. The original unit of GEOS-
162 Chem-simulated O₃ is ppb, which was converted to μg m⁻³ assuming a constant temperature of 25°C and pressure of
163 1013.25 hPa (1 μg m⁻³ is approximately 0.5 ppb) when compared with observations (Yin et al., 2017b; Gong and Liao,
164 2019).

165 Global anthropogenic emissions of CO, NO_x, SO₂ and VOCs are from Community Emissions Data System (CEDS),
166 which has coverage over the simulation years of 1950–2014 (Hoesly et al., 2018). Biomass burning emissions are from the
167 GFED-4 inventory (Van Der Werf et al., 2017). Biogenic VOC emissions are computed by the Model of Emissions of
168 Gases and Aerosols from Nature (MEGAN) v2.1 (Guenther et al., 2012), which is embedded in GEOS-Chem. Emissions
169 of biogenic VOC species in each grid cell, including isoprene, monoterpenes, methyl butenol, sesquiterpenes, acetone and
170 various alkenes, are simulated as a function of canopy-scale emission factors modulated by environmental activity factors
171 to account for changing temperature, light, leaf age, leaf area index (LAI), soil moisture and CO₂ concentrations
172 (Sindelarova et al., 2014).

173 Dry deposition follows the resistance-in-series scheme of Wesely (1989), which depends on species properties, land
174 cover types and meteorological conditions, and uses the Olson land cover classes with 76 land types reclassified into 11
175 land types. Although transpiration is a potential mechanism via which the land cover affects ozone, we do not address it in
176 this study because water vapor concentration in GEOS-Chem is prescribed from assimilated relative humidity (i.e., not
177 computed online from evapotranspiration).

178 **2.3 LightGBM machine-learning model**

179 In this study, we used the LightGBM algorithm to integrate GEOS-Chem simulated O₃ at a lower resolution with
180 higher-resolution multi-source data to produce higher-resolution hourly O₃ and MDA8-O₃ fields. Because the
181 representation of input data for LightGBM should be regular, datasets at different spatial resolutions were all regridded to
182 a unified resolution of 0.25°×0.25°, consistent with the meteorological fields. By taking the advantage of these high-
183 resolution datasets, the hybrid approach can not only correct the biases of the GEOS-Chem-simulated O₃, but also refine it
184 into a finer resolution. LightGBM is a ML algorithm based on the gradient boosting decision tree (Chen and Guestrin,
185 2016), which has a high training efficiency and lower memory footprint, and thus is suitable for processing massive high-
186 dimensional data (Zhang et al., 2019). The general steps to build a ML model can be summarized as follows: (1) choose
187 an algorithm appropriate for the problem (e.g., regression or classification); (2) clean the data and split them into training
188 and test data; (3) train and tune the model with training data to well capture prediction patterns; (4) evaluate model
189 performance on test data; and (5) return to step (3) and (4) until an optimal predictive ability is reached. The whole dataset
190 is divided into training and test data to evaluate the model generalization ability. The model performance on test data can
191 indicate whether the model can perform well on new data independent of the training process. A timescale of a year has
192 been suggested to strike a good balance between computational burden and utility for air quality forecasting, as the
193 variability in the power spectrum of surface O₃ can be captured by timescales of a year or less (Ma et al., 2021). Thus, in
194 this study, data for 2016–2017 were used as the training data, and data for 2018 were used as the independent test data. In
195 any process involving comparison with O₃ observations at site, the data or results from the nearest grid cells were used.

196 During the model training process, the model was evaluated with 10-fold cross-validation to ensure the robustness
197 and reliability of the model, whereby the training data were randomly partitioned into 10 subsets of approximately the same



198 size, with 90% of data used to train individual models and the ensemble model, and the remaining 10% of data used to
199 examine model performance (Xiao et al., 2018). This process was repeated 10 times so that each data record was left for
200 testing once. The tuning of the hyperparameters was optimized using grid search optimization to improve detection
201 performance and diagnostic accuracy (Wang et al., 2019). Statistical indicators, including the coefficient of determination
202 (R^2) and root-mean-square error (RMSE), were used in subsequent assessment of model performance for GEOS-Chem
203 alone and for the hybrid approach.

204 2.4 Ozone exposure metric and dose–response functions

205 Among O_3 exposure indices, AOT40 has been used widely during the last two decades as it has been found to have a
206 strong relationship with relative yield of many crop species (Mills et al., 2007), and thus was used to quantify the impacts
207 of surface O_3 on crop yields in this study. The flux-based metrics, which require long-term simulations using a process-
208 based stomatal uptake model, were beyond the scope of this study. The AOT40 (ppm-h) is defined as follows:

$$209 \quad AOT40 = \sum_{i=1}^n ([O_3]_i - 0.04) \quad (1)$$

210 where the $[O_3]_i$ is the hourly mean O_3 concentration (ppm) during the 12 hours of local daytime (08:00–19:59); n is the
211 number of hours in the growing season defined as the 90 days prior to the start of the harvesting period according to the
212 crop calendar.

213 The exposure–response functions based on extensive field experimental studies have been established to relate a
214 quantifiable O_3 -exposure metrics to crop yields. It has been suggested that , suggesting greater RYL responses found in
215 Asian experiments than the American and European counterparts, and possibly higher O_3 sensitivity of Asian crop varieties
216 (Emberson et al., 2009; Feng et al., 2022). To better understand O_3 -induced risks to crops in China, the AOT40 dose–yield
217 functions developed based on field experiments in China are used in this study, which are named as AOT40-China. The
218 dose–response functions for soybean is from Zhang et al. (2017), and for other three crops are from Feng et al. (2022). The
219 statistical dose–yield relationships used in this study are summarized in **Table S1**.

220 2.5 Analysis of health impacts

221 All-cause mortality, cardiovascular disease mortality and respiratory disease mortality are selected as the health
222 outcomes of our study due to the high correlation between these endpoints and short-term O_3 exposure in previous studies.
223 A log-linear exposure–response function is widely adopted and recommended by the World Health Organization (WHO)
224 for health impact assessment in areas with severe air pollution. In particular, the log-linear model is the most widely applied
225 exposure–response model at present in China (Lelieveld et al., 2015; Yin et al., 2017a; Zhang et al., 2022b). The premature
226 mortality is calculated following:

$$227 \quad \Delta M = \delta c * \left[\frac{(RR - 1)}{RR} \right] * P \quad (2)$$

228 where ΔM is the excess mortality attributable to O_3 exposure; δc is the baseline mortality rate for a particular health endpoint
229 (Yin et al., 2017b; Madaniyazi et al., 2016); P is the exposed population; and RR is the relative risk defined as:

$$230 \quad RR = \exp((X - X_0) * \beta) \quad (3)$$

231 where β is the exposure–response coefficient derived from epidemiological cohort studies (Shang et al., 2013); X represents
232 the model-calculated O_3 concentration; the value of X_0 is the threshold concentration below which no additional risk is
233 assumed. Consistent with previous studies (Lelieveld et al., 2015; Liu et al., 2018), we used $X_0 = 75.2 \mu g m^{-3}$.

234 In this study, the mean MDA8- O_3 concentrations in warm season (May–September) were used to estimate the disease-
235 specific health impacts of short-term exposure to O_3 . The province-level population and national baseline mortality rate for



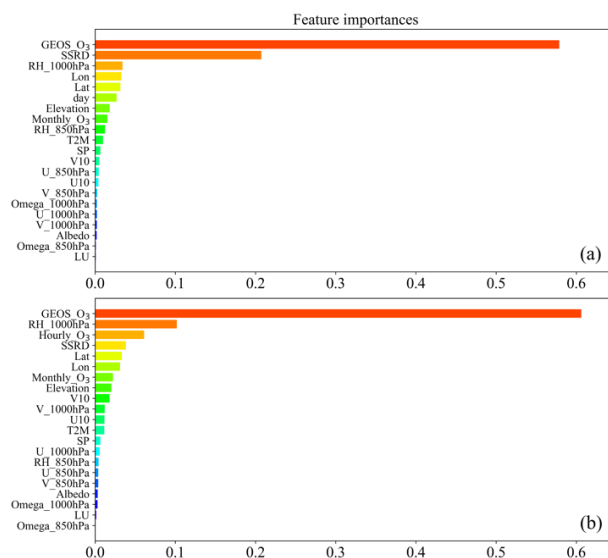
236 particular diseases were provided by the National Bureau of Statistics (<http://www.stats.gov.cn/>). The spatial differences of
 237 baseline mortality in China were not considered without provincial-level data, which means that we assume the baseline
 238 mortality is evenly distributed across China (Dedoussi et al., 2020). The exposure-response coefficients were obtained from
 239 existing epidemiological studies in China (**Table S2**). If the corresponding coefficient of a province could not be found in
 240 published epidemiological studies, the datum closest to that province would be selected as a substitute. If there were no
 241 neighboring provinces, the results of national meta-analysis would be used (Zhang et al., 2021).

242 3 Results

243 3.1 Model development and validation

244 The finally selected features and their importance estimated by the LightGBM algorithm based on 10-fold cross
 245 validation are shown in **Fig. 2**. GEOS-Chem-simulated O₃ is the top predictor for predicting surface O₃ concentrations,
 246 accounting for 61% and 58% of all relative importance in the ML algorithm predicting hourly O₃ and daily MD8A-O₃,
 247 respectively. The result indicates that process-based GEOS-Chem simulations have high utility for O₃ predictions under
 248 the hybrid approach (Ma et al., 2021). The meteorological variables with high contribution to both the daily and hourly
 249 models are downward surface solar radiation (SSRD), relative humidity at 1000 hpa (RH_1000hpa) and 10-m horizontal
 250 wind (U10 and V10). Other special features, including location (latitude and longitude), elevation and diurnal and monthly
 251 pattern of O₃, also contribute to ambient O₃ estimations. The spatial distributions of bias-corrected O₃ are consistent with
 252 observations for both training and test datasets (**Fig. S1**), indicating that there is no obvious overfitting, i.e., the model is
 253 able to generalize from the training set to the test set. The good generalization ability of the model gives us confidence in
 254 its ability to make accurate predictions based on new data. In general, the hybrid approach can yield good O₃ estimates in
 255 the data-intensive regions, including eastern and central China that are the hotspot areas of O₃ pollution.

256



257

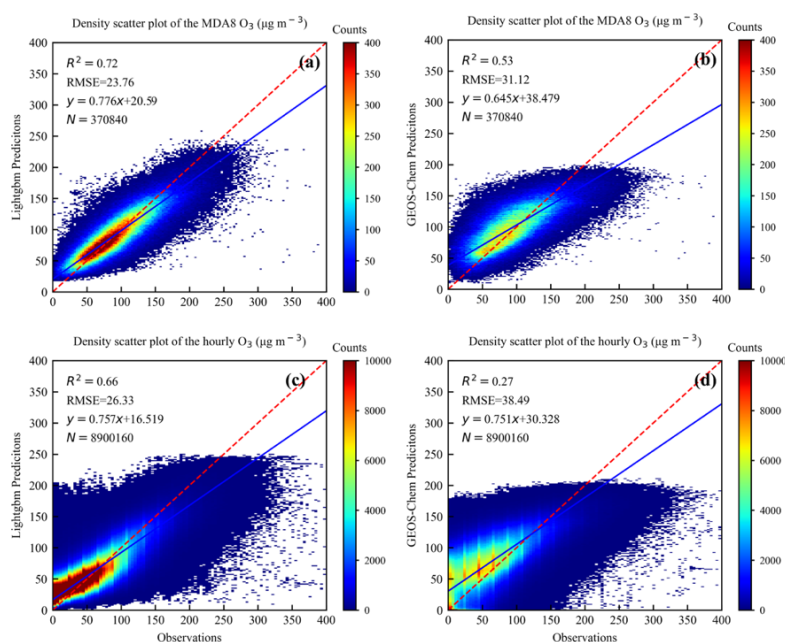
258 **Figure 2. The feature importance plot for (a) MDA8-O₃ and (b) hourly O₃, respectively. The full list of candidate**
 259 **variables with their symbols, units, descriptions, and data sources are shown in Table S1.**

260



261 **Fig. 3** shows the density scatter plots between O₃ measurements and GEOS-Chem simulations, as well as the hybrid-
 262 approach predictions for 2018. The R^2 value of the hybrid approach and GEOS-Chem model are 0.66 and 0.27 at hourly
 263 level, and 0.72 and 0.53 at MDA8-O₃ level, respectively. Bias-corrected O₃ concentrations have lower RMSE in
 264 comparison with GEOS-Chem simulated O₃ concentrations, reduced from 31.1 to 23.8 $\mu\text{g m}^{-3}$ for MDA8-O₃ predictions,
 265 and from 38.5 to 26.3 $\mu\text{g m}^{-3}$ for hourly predictions. The MDA8-O₃ model performance is better than that of the hourly
 266 model, indicating reduced errors upon temporal averaging. The result suggests that the CTM-simulated results can be
 267 substantially improved by applying ML with multi-source datasets, and the bias-corrected data can improve our
 268 understanding of long-term O₃ trends and its further implications on crop and human health over China, as discussed in the
 269 following sections.

270 In comparison with previous studies, Liu et al. (2020) used XGBoost to predict O₃ in major urban areas of China at a
 271 resolution of $0.1^\circ \times 0.1^\circ$, and the R^2 value and RMSE for MDA8-O₃ were 0.74 and 23.8 $\mu\text{g m}^{-3}$, respectively. Their result
 272 indicates that higher-resolution predictions may help enhance model accuracy, but represent a trade-off between model
 273 accuracy and time efficiency depending on the purpose. Instead of directly predicting O₃ concentrations, Ivatt and Evans
 274 (2020) predicted biases in GEOS-Chem-simulated O₃ concentrations and then corrected them with XGBoost. They also
 275 suggested that the corrected model performs considerably better than the uncorrected model, with RMSE reduced from
 276 16.2 to 7.5 ppb and Pearson's R raised from 0.48 to 0.84. Their greater improvement with larger reduced RMSE than our
 277 result is mainly because they selected fewer sites for training, with all the urban and mountain sites (observations made at
 278 a pressure < 850 hPa) removed. The removal of these sites can improve the overall apparent performance of the model
 279 because O₃ formation could have different characteristics in these areas. In general, ML methods have been proven to be a
 280 promising tool to improve air pollutant forecasts when a process-level understanding is still incomplete.



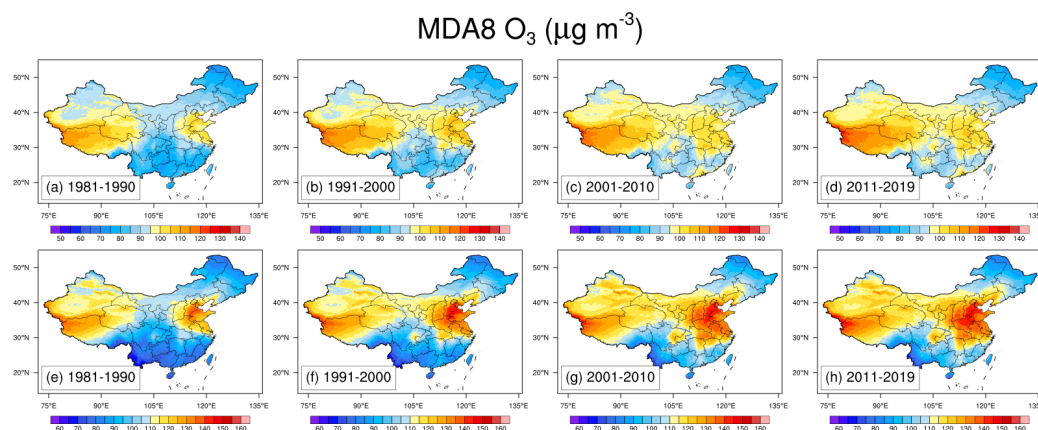
281
 282 **Figure 3.** Density scatter plots and linear regression statistics of O₃ predictions vs. observation for 2018: (a) bias-
 283 corrected MDA8-O₃ vs. observations; (b) GEOS-Chem MDA8-O₃ vs. observations; (c) bias-corrected hourly O₃ vs.
 284 observations; and (d) GEOS-Chem hourly O₃ vs. observations. The dashed red line indicates the 1:1 line, and the
 285 solid blue line indicates the line of best fit using orthogonal regression. The R^2 is the coefficient of determination,



286 RMSE is the root-mean-square error, and N is the number of data points. The X and Y axis represents the O₃
 287 observations and predictions, respectively.
 288

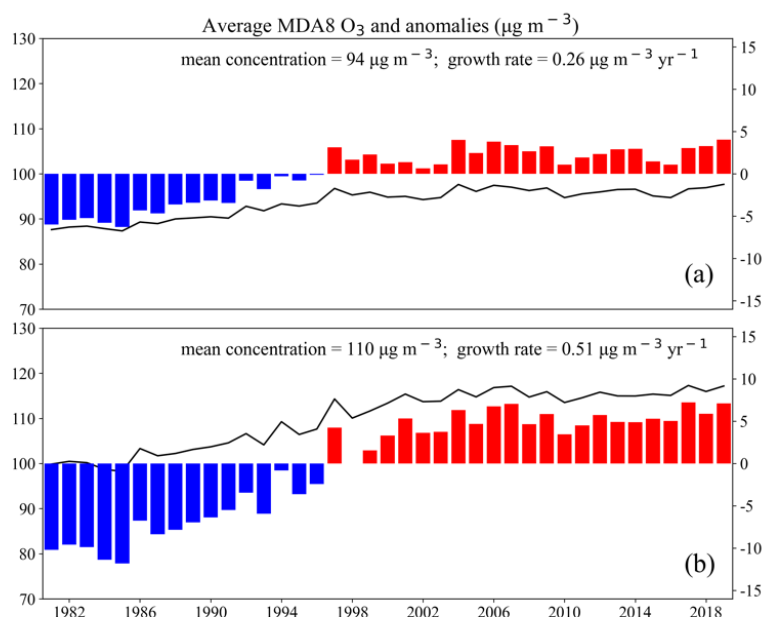
289 3.2 Spatiotemporal distribution and trends of O₃ predictions

290 **Fig. 4** demonstrates the spatial patterns of averaged annual and warm-season (May-September) MDA8-O₃ from 1981
 291 to 2019. When compared to the high concentrations in the warm season, MDA8-O₃ concentrations are relatively lower at
 292 annual level. The annual and warm-season MDA8-O₃ concentrations have similar spatial distribution, and both present an
 293 increasing trend over the past decades, with more substantial increase observed between 1981 and 2010. The O₃ levels in
 294 southern China are lower than those in northern China, but they are still relatively high in the PRD region, which is
 295 consistent to findings in previous studies (e.g. Liu and Wang, 2020b). During the first decade of 1981–1990, high O₃
 296 concentration areas are mainly concentrated in the BTHs and northern Shandong. In the next two decades, O₃ pollution
 297 extensively expands to most of East and North China, spreading northward to Jilin and Liaoning, westward to Shanxi and
 298 Ningxia, and southward to northern Hunan, Shanxi and Zhejiang. Moreover, the SCB and PRD regions also experience
 299 aggravated O₃ pollution during this period. In the last decade of the study period, O₃ concentrations remain at high levels
 300 in BTHs and SCB without obvious changes. To understand the detailed changes and trends of O₃, next we analyze the
 301 interannual variability.



302
 303 **Figure 4. Spatial distribution of the annual mean MDA8-O₃ concentrations ($\mu\text{g m}^{-3}$) during: (a) 1981–1990; (b)**
 304 **1991–2000; (c) 2001–2010; and (d) 2011–2019. Spatial distribution of the warm-season (May–September) mean**
 305 **MDA8-O₃ concentrations of (e)1981–1990, (f) 1991–2000, (g) 2001–2010; and (h) 2011–2019.**

306 **Fig. 5** shows that the annual averaged MDA8-O₃ concentrations increase from $87 \mu\text{g m}^{-3}$ in 1981 to $98 \mu\text{g m}^{-3}$ in
 307 2019, with a growth rate of $+0.26 \mu\text{g m}^{-3} \text{ yr}^{-1}$, while the warm-season averaged MDA8-O₃ concentrations increase from
 308 $100 \mu\text{g m}^{-3}$ in 1981 to $117 \mu\text{g m}^{-3}$ in 2019, having a growth rate of $+0.51 \mu\text{g m}^{-3} \text{ yr}^{-1}$. Moreover, the average annual and
 309 warm-season O₃ concentrations have a more obvious upward trend before 2000s, with a growth rate of $0.38 \mu\text{g m}^{-3} \text{ yr}^{-1}$
 310 and $0.71 \mu\text{g m}^{-3} \text{ yr}^{-1}$, compared to that after 2000s, when O₃ concentrations appear to fluctuate within a certain range.
 311 GEOS-Chem-simulated O₃ has a similar trend as the bias-corrected O₃, but it generally overestimates O₃ concentrations on
 312 national scale (**Fig. S2**). The annual and warm-season averaged MDA8-O₃ concentrations in BTHs, YRD, SCB and PRD
 313 regions are shown in **Fig. S3–S4**. The warm-season increasing trend for BTHs, YRD, SCB and PRD regions are $0.32 \mu\text{g m}^{-3} \text{ yr}^{-1}$,
 314 $0.63 \mu\text{g m}^{-3} \text{ yr}^{-1}$, $0.84 \mu\text{g m}^{-3} \text{ yr}^{-1}$, and $0.81 \mu\text{g m}^{-3} \text{ yr}^{-1}$ from the year 1981 to 2019.



315

316 **Figure 5. The bias-corrected MDA8-O₃ predictions (black line; left y axis) and corresponding anomalies (colored**
 317 **bar; right y axis) from 1981 to 2019: (a) annual mean; and (b) warm-season mean (May-September). The trends**
 318 **(growth rates) are obtained by ordinary linear regression on mean values of MDA8-O₃. The anomalies are defined**
 319 **as annual mean minus the multidecadal average over 1981–2019.**

320 In recent years, the worsening O₃ pollution has fueled numerous studies on ground-level O₃ spatial distribution and
 321 changes in China, which were conducted on local, regional and national scale using different O₃ fields from observations,
 322 CTMs and ML estimates. In this study, we mainly focus on the regional and national O₃ characteristics, and the reported
 323 O₃ trends in recent studies are listed in **Table 1**. By comparing the results of existing works, we find that source-varied O₃
 324 fields can induce great uncertainty of the O₃ trends. Moreover, the O₃ trends are found to be very sensitive to the study
 325 period even with the same O₃ fields (Wei et al., 2022), which indicates large interannual variability, mostly reflecting the
 326 changing anthropogenic emissions and meteorology (Lu et al., 2019; Li et al., 2020). In contrast to the perceptible O₃ trends,
 327 Liu et al. (2020) suggested that O₃ pollution in most parts of China has only modest changes between 2005 and 2017, and
 328 their trends were not spatially continuous. Wang et al. (2022b) also reported that O₃ has small positive increase rates for
 329 2013–2021 in many cities, and the O₃ increase rates greatly differ from site to site even within the same region.

330 In comparison, our results indicate no obvious increasing trends of national MDA8-O₃ within the same study period
 331 (**Fig. 5**). On a regional scale, only BTHs have a perceptible increasing trend in more recent years, while no such trends are
 332 found over the YRD, SCB and PRD regions during the same period. The summertime MDA8-O₃ in BTHs has a change
 333 rate of +0.81 µg m⁻³ yr⁻¹, which is much lower than the results using O₃ observations (Li et al., 2020). One possible reason
 334 is that most observational sites are in urban regions, which usually suffer more serious O₃ pollution, while the O₃
 335 concentrations from model simulations and ML methods are calculated on the scale of a grid cell with lower domain-
 336 averaged values. Moreover, gridded data at a relatively coarse resolution may fail to capture larger site differences, leading
 337 to the larger discrepancy of between O₃ observations and gridded O₃ estimates.



338 **Table 1 Summary of reported regional and national MDA8-O₃ trends (µg m⁻³ yr⁻¹).**

Region	Period	Increase rate	Data source/Method	References
Nation	2013–2017 (annual)	0.35	ML (XGBoost)	(Liu et al., 2020)
	2013–2017 (annual)	0.92	WRF-CMAQ	(Liu and Wang, 2020a)
	2013–2017 (annual)	1.33	ML (ERT)	(Wei et al., 2022)
	2015–2019 (annual)	4.40	ML (ERT)	(Wei et al., 2022)
	2015–2019 (annual)	1.90	Observations	(Maji and Namdeo, 2021)
	2013–2019 (summer)	3.80	Observations	(Li et al., 2020)
	1981–2019 (annual)	0.26	ML (LightGBM)	This study
	1981–2000 (annual)	0.38	ML (LightGBM)	This study
	1981–2019 (warm-season)	0.51	ML (LightGBM)	This study
BTH	1981–2000 (warm-season)	0.71	ML (LightGBM)	This study
	2010–2017 (annual)	0.60	ML (Random Forest)	(Ma et al., 2021)
	2013–2017 (annual)	1.33	ML (XGBoost)	(Liu et al., 2020)
	2013–2017 (annual)	4.78	ML (ERT)	(Wei et al., 2022)
	2012–2017 (summer)	1.16	GEOS-Chem	(Dang et al., 2021)
	2013–2019 (summer)	6.60	Observations	(Li et al., 2020)
	1981–2019 (summer)	0.46	ML (LightGBM)	This study
	2013–2019 (summer)	0.81	ML (LightGBM)	This study
	YRD	2013–2017 (annual)	2.94	ML (ERT)
2015–2019 (annual)		5.60	ML (ERT)	(Wei et al., 2022)
2012–2017 (summer)		3.48	GEOS-Chem	(Dang et al., 2021)
2013–2019 (summer)		3.20	Observations	(Li et al., 2020)
1981–2019 (annual)		0.24	ML (LightGBM)	This study
1981–2019 (summer)		0.73	ML (LightGBM)	This study
SCB	2013–2017 (annual)	2.37	ML (ERT)	(Wei et al., 2022)
	2013–2019 (summer)	1.40	Observations	(Li et al., 2020)
	1981–2019 (annual)	0.48	ML (LightGBM)	This study
	1981–2019 (summer)	0.98	ML (LightGBM)	This study
PRD	2007–2017 (annual)	1.20	Observations	(Yang et al., 2019)
	2013–2017 (annual)	-0.72	ML (ERT)	(Wei et al., 2022)
	2015–2019 (annual)	4.38	ML (ERT)	(Wei et al., 2022)
	2013–2019 (summer)	2.20	Observations	(Li et al., 2020)
	1981–2019 (annual)	0.56	ML (LightGBM)	This study
	1981–2019 (fall)	0.69	ML (LightGBM)	This study

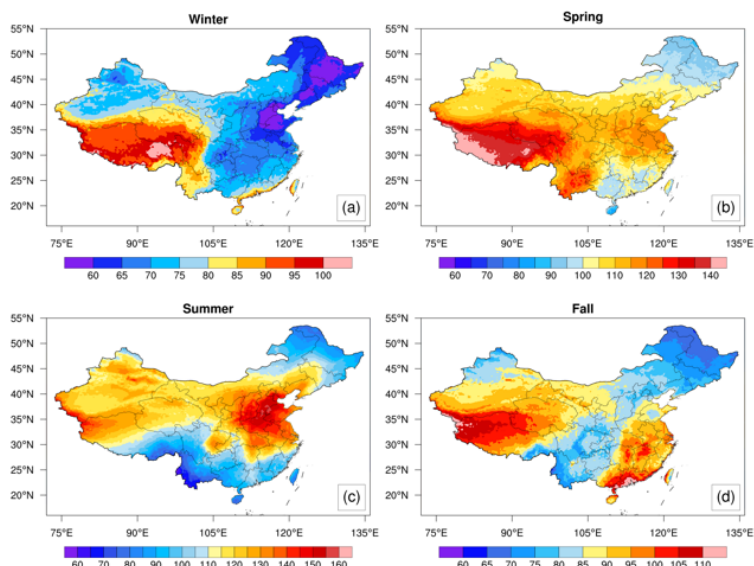
339

340 **3.3 Seasonal characteristics of O₃ predictions**

341 Differences in averaged annual and warm-season O₃ concentrations indicate that O₃ has distinctive seasonal
 342 characteristics. **Fig. 6a-d** shows the seasonal variations in O₃ concentrations from 2011–2019, and results for other past
 343 three decades are shown in **Fig. S5-S7**. In winter, pollution is mainly concentrated in the coastal areas of southern China.
 344 In spring, O₃ pollution primarily occurs in eastern China and the southern part of Yunnan Province. O₃ pollution continues
 345 to aggravate over eastern China in summer, particularly in BTHs, and further extends to SCB. The air quality in eastern
 346 and central China is greatly improved in fall, while southern China experiences the most pollution in this period. In general,
 347 the peak and trough values of O₃ concentrations appear in summer and winter, respectively. However, O₃ concentrations
 348 are found to be minimum in summer and maximum in fall over PRD, which is largely determined by the summer monsoon
 349 (Zhou et al., 2013; Wang et al., 2018). **Fig. S8** shows the seasonal averaged MDA8-O₃ concentrations in different regions
 350 from 1981 to 2019. In winter, O₃ concentrations do not have much change across the four regions over the past decades,
 351 staying mostly between 70–80 µg m⁻³. Moreover, wintertime O₃ concentrations after the 2000s are generally lower than
 352 that before the 2000s in BTHs, YRD and SCB. In contrast, summertime O₃ concentrations have a dramatic increase over
 353 the four regions. In spring and fall, O₃ concentrations have an increasing trend in PRD, while it mostly fluctuates within a



354 certain range in the other three regions. The results show that O₃ in non-winter seasons has a more pronounced increase
 355 during 1981–2019 albeit with regional differences. The regional characteristics of O₃ and its influencing factors will be
 356 further discussed in Section 3.4.



357
 358 **Figure 6. Spatial distribution of the bias-corrected MDA8-O₃ predictions ($\mu\text{g m}^{-3}$) from 2011–2019: (a) winter; (b)**
 359 **spring; (c) summer; and (d) fall.**

360 3.4 Regional characteristics of O₃ predictions

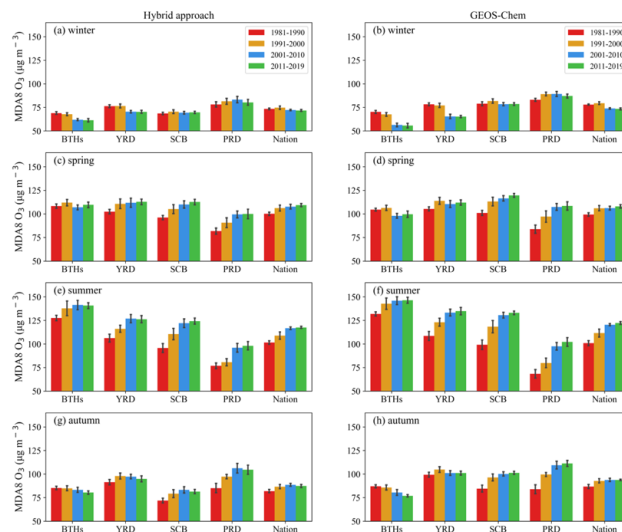
361 **Fig. 7** shows the bar plots of the seasonal MDA8-O₃ concentrations in each region from 1981–2019 for bias-corrected
 362 and GEOS-Chem-simulated O₃. For the bias-corrected O₃, the averaged summertime MDA8-O₃ concentrations in BTHs,
 363 YRD, SCB and fall-time MDA8-O₃ concentrations in PRD are $137 \pm 8 \mu\text{g m}^{-3}$, $119 \pm 10 \mu\text{g m}^{-3}$, $113 \pm 12 \mu\text{g m}^{-3}$ and $98 \pm$
 364 $10 \mu\text{g m}^{-3}$, with the increasing rate being $0.46 \mu\text{g m}^{-3} \text{yr}^{-1}$, $0.73 \mu\text{g m}^{-3} \text{yr}^{-1}$, $0.98 \mu\text{g m}^{-3} \text{yr}^{-1}$ and $0.69 \mu\text{g m}^{-3} \text{yr}^{-1}$ from 1981
 365 to 2019, respectively (**Fig. S9**). For GEOS-Chem-simulated O₃, the averaged summertime MDA8-O₃ concentrations in
 366 BTHs, YRD, SCB and fall-time MDA8-O₃ concentrations in PRD are $141 \pm 7 \mu\text{g m}^{-3}$, $125 \pm 11 \mu\text{g m}^{-3}$, $120 \pm 14 \mu\text{g m}^{-3}$
 367 and $100 \pm 12 \mu\text{g m}^{-3}$, respectively. It shows that O₃ concentrations of the four regions have a consistent upward trend in
 368 the summer over the past decades, but there are regional differences in other seasons. Compared to BTHs and YRD, PRD
 369 and SCB have more distinctive O₃ increases in spring and fall. Among these four regions, the O₃ concentrations in BTHs
 370 has the biggest seasonal differences, but have the smallest seasonal differences in PRD.

371 The spatiotemporal patterns of O₃ in China have been proven to largely depend on both emissions and meteorology.
 372 The regional O₃ pollution is usually found to be triggered by specific circulation patterns as local meteorological factors
 373 are modulated by synoptic-scale circulation patterns. China has a large territory and is affected by different weather systems.
 374 The continental high-pressure systems, components of East Asian summer monsoon (EASM) and tropical cyclones, among
 375 others, are critical synoptic conditions leading to O₃ formation and transport in China (Wang et al., 2022b; Han et al., 2020).
 376 For instance, regional O₃ pollution in North China usually occurs under a typical weather pattern of an anomalous high-
 377 pressure system at 500 hPa (Gong and Liao, 2019), which creates favorable meteorological conditions for high O₃ levels
 378 with high temperature, low relative humidity, anomalous southerlies and divergence in the lower troposphere. As one of
 379 the most important components of EASM, the Western Pacific subtropical high (WPSH) strongly influences summertime
 380 precipitation and atmospheric conditions in East China. A strong WPSH can decrease O₃ levels over YRD as enhanced



381 moisture is transported into YRD under prevailing southwesterly winds (Zhao and Wang, 2017). Located on the southern
 382 coast of China, PRD features a typical subtropical monsoon climate. There O₃ concentrations are usually the lowest in
 383 summer due to the prevailing southerlies with clean air from the ocean and the associated large rainfall, while the worst O₃
 384 pollution usually happens in fall mainly due to the occasional northerly winds during the monsoonal transition, thereby
 385 importing precursors from the north, and stable and still relatively warm and sunny weather conditions before the winter
 386 starts. Downdrafts in the periphery circulation of a typhoon system can also strongly enhance surface O₃ before typhoon
 387 landing (Jiang et al., 2015; Lu et al., 2021; Li et al., 2022). On one the hand, the poor ventilation in the peripheral subsidence
 388 region of typhoons favors the accumulation of O₃ and its precursors. On the other hand, the deep subsidence can transport
 389 the O₃ in the upper troposphere and lower stratosphere to surface, causing aggravated O₃ pollution. Moreover, smaller-
 390 scale circulation patterns, such as land-sea and mountain-valley breezes, also influence O₃ in coastal regions (Ding et al.,
 391 2004; Zhou et al., 2013; Wang et al., 2018).

392 When compared to the hybrid approach, GEOS-Chem generally has similar O₃ distribution and trends over each
 393 region, while overestimating O₃ concentrations (Table S1). GEOS-Chem particularly overestimates wintertime and fall-
 394 time O₃ concentrations in SCB, which are $10 \pm 1 \mu\text{g m}^{-3}$ and $17 \pm 3 \mu\text{g m}^{-3}$ higher than those of the hybrid approach,
 395 respectively. Previous studies reported such model overestimates and proposed a number of explanations involving
 396 precursor emissions, dry deposition, and vertical mixing in the planetary boundary layer (PBL), etc. Both observational
 397 analyses and inter-model comparisons suggested that the summertime dry deposition of O₃ calculated by the Wesely
 398 scheme in GEOS-Chem could be underestimated, which has been invoked as a cause for model overestimates of O₃. The
 399 biased emissions in the model, as consistent with the biased-high tropospheric NO_x columns, result in overestimated O₃.
 400 Travis et al. (2016) showed that GEOS-Chem with reduced NO_x emissions provides an unbiased simulation of O₃
 401 observations from the aircraft and reproduces the observed O₃ production efficiency in the boundary layer. Lin et al. (2008)
 402 suggested that the excessive PBL mixing can lead to the biased-high O₃ concentrations. The fully mixed O₃ throughout the
 403 PBL means that the higher O₃ concentrations in the upper PBL are brought down to the surface much more efficiently.
 404 Moreover, the excessive spatial averaging of emissions at coarser resolutions could also lead to systematic overestimation
 405 of regional O₃ production (Wang et al., 2013). In summary, with a higher prediction accuracy, the hybrid approach lends
 406 greater credence to using model simulations to extrapolate historical O₃ further back in time, which can furthermore provide
 407 us with more accurate estimates of O₃ impacts on crop production and human health.



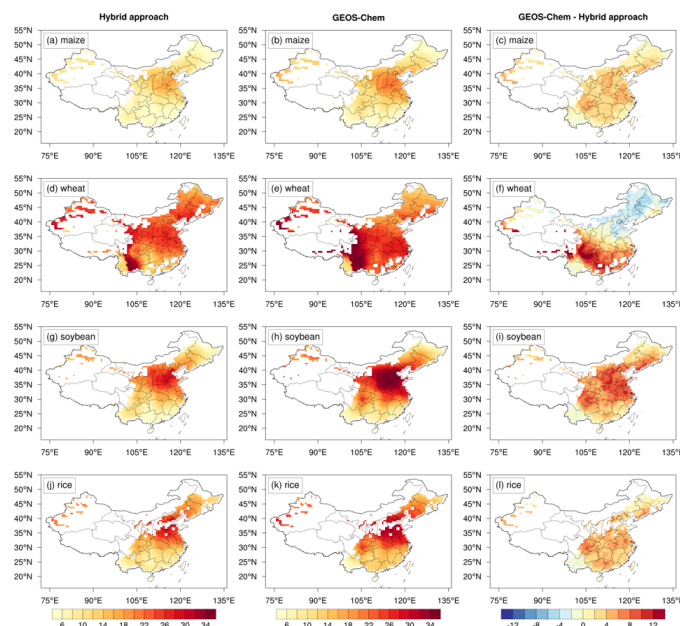
408
 409 **Figure 7. The seasonal mean MDA8-O₃ concentrations ($\mu\text{g m}^{-3}$) in different regions during 1981-2019. Bias-**



410 corrected MDA8-O₃ in: (a) winter; (c) spring; (e) summer; and (g) fall. GEOS-Chem MDA8-O₃ in: (b) winter; (d)
411 spring; (f) summer; and (h) fall. The error bar represents the standard deviation.

412 3.5 Crop production losses attributable to O₃ pollution

413 **Fig. 8** shows the relative yield losses (RYLs; $RYL = 1 - RY$, where RY is the relative yield defined as the ratio of the
414 O₃-affected yield to the yield without O₃ exposure) calculated with GEOS-Chem and bias-corrected O₃ using AOT40-
415 China metric. For a given crop, the RYLs show generally consistent spatial distribution across the metrics, with BTHs
416 having the most serious crop yield losses due to high O₃ concentrations. Compared to the bias-corrected O₃, using GEOS-
417 Chem-simulated O₃ generally leads to larger yield losses, especially over BTHs and SCB, reflecting overestimated O₃
418 concentrations by GEOS-Chem in cropland areas during the growing seasons (**Fig. S11**), primarily in spring and summer,
419 which is consistent to the above analysis. GEOS-Chem-simulated O₃ leads to slightly underestimated wheat yield loss only
420 over some parts of BTHs, mostly because the primary growing period of wheat there is in winter and spring, and GEOS-
421 Chem has lower O₃ estimates than the hybrid approach during this period there (**Table S2**).



422 **Figure 8.** Estimated annual mean relative yield losses (RYLs, in %) of four staple crops from 1981–2019 using the
423 AOT40-China metric. The estimated RYLs using bias-corrected O₃: (a) maize; (d) wheat; (g) soybean; and (j) rice.
424 The estimated RYLs using GEOS-Chem-simulated O₃: (b) maize; (e) wheat; (h) soybean; and (k) rice. The
425 differences in estimated RYLs between GEOS-Chem-simulated and bias-corrected O₃: (c) maize; (f) wheat; (i)
426 soybean; and (l) rice. The GEOS-Chem-simulated O₃ were regridded to 0.5°×0.5° for comparison with bias-
427 corrected O₃.
428

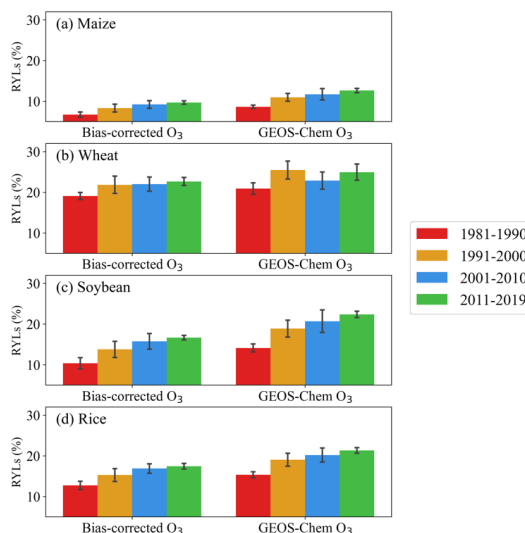
429 **Fig. 9** shows the bar plots of the relative yield for each crop using AOT40-China dose-yield relationship. Crop yield
430 losses are generally consistent with the O₃ trends as the dose-yield relationships used here are essentially a set of linear
431 functions. Most crops experience aggravated yield losses over the past four decades due to enhanced O₃ concentrations,
432 except for wheat, which has the largest yield loss during the period 1991 to 2000. The reason could be that BTHs have the



433 highest O₃ concentrations in spring during the 1990s (**Fig. S10**), which is the primary growing season for wheat. Noticeable
 434 uncertainties of crop yield losses are found across metrics.

435 The average annual crop RYLs from 1981 to 2019 for wheat, rice, soybean and maize range from 1.1 to 13.4%, 2.7 to
 436 13.4%, 6.3 to 24.8% and 0.8 to 7.4%, respectively. The differences in yield losses across crops reflect the dependence on
 437 crop-specific phenology and ecophysiology. The estimated annual RYLs using bias-corrected O₃ for wheat, rice, soybean
 438 and maize from 1981 to 2019 range from 17.5–25.5%, 10.7–19.1%, 7.3–17.9% and 7.1–12.7%, with a growth rate of 0.03%
 439 yr⁻¹, 0.04% yr⁻¹, 0.27% yr⁻¹ and 0.13% yr⁻¹. Wheat is the most sensitive crop to the O₃ concentrations, whereas maize is
 440 the least sensitive. Using GEOS-Chem-simulated O₃, the estimated annual RYLs for wheat, rice, soybean and maize from
 441 1981 to 2019 are 18.7–28.7%, 14.0–22.0%, 12.4–23.1%, and 7.9–13.2%, having a growth rate of 0.08% yr⁻¹, 0.14% yr⁻¹,
 442 0.23% yr⁻¹ and 0.11% yr⁻¹. There are noticeable differences in crop yield estimates using the bias-corrected and GEOS-
 443 Chem O₃, indicating again the importance of the bias-corrected high-resolution O₃ data in related crop issues.

444 In existing studies evaluating the O₃-induced crop losses in China, which also use dose-yield relationship derived from
 445 the experiments conducted in Asia, Zhang et al. (2017) reported that the ambient O₃ concentrations in Northeast China
 446 cause substantial annual yield loss of soybean ranging from 23.4% to 30.2% during 2013 and 2014, depending on the O₃
 447 metric used (including AOT40, W126, SUM06 and a flux-based metric). Feng et al. (2022), using AOT40, indicated that
 448 the annual average RYLs of wheat (33%), rice (23%) and maize (9%) from 2017 to 2019. Our correspondingly estimated
 449 RYLs for rice (18.0%) and maize (10.0%) are generally consistent to their results, while the RLYs for soybean (16.4%)
 450 and wheat (23.4%) are much lower than the estimates. Since we used the same dose-response relationships in their studies,
 451 the discrepancies are primarily attributed to the differences in used metrics (only for soybean), O₃ fields and sensitivity of
 452 crop to the changes of O₃ concentrations (Mukherjee et al., 2021; Feng et al., 2022; Mills et al., 2018). In Zhang et al.
 453 (2017), the O₃ measurements are obtained from the experimental field (45°73'N, 126°61'E), and in Feng et al. (2022), the
 454 measured O₃ concentrations are from over 3,000 monitoring sites across East Asia. The results of comparison are consistent
 455 to the previous analysis of O₃ trends and variability from different sources, where the domain-average values of O₃
 456 observations are larger than gridded O₃ from model simulations (**Section 3.2**) and thus lead to larger estimates of RYLs.
 457 On one hand, it indicates that O₃ fields should be considered as a great source of uncertainty when comparing the results
 458 of previous studies using source-varied O₃ fields. Moreover, different degrees of importance should be given for specific
 459 crops, for example, the changes in O₃ concentrations have a larger impact on wheat crop. On the other hand, it highlights
 460 again the necessity and importance of bias correction for model-simulated O₃ when O₃-induced crop reduction.



461

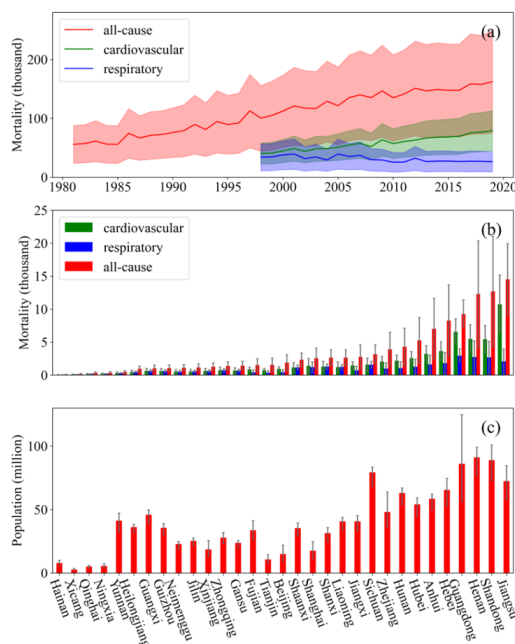


462 **Figure 9. The estimated decadal mean relative yield losses (RYLs) of four staple crops using different metrics from**
463 **1981–2019. The estimated RYLs using bias-corrected O₃: (a) maize; (c) wheat; (e) soybean; and (g) rice. The**
464 **estimated RYLs using GEOS-Chem-simulated O₃: (b) maize; (d) wheat; (f) soybean; and (h) rice. The error bar**
465 **represents the standard deviation.**

466 3.6 Health impacts attributable to O₃ pollution

467 The exposure-response coefficients for the short-term, acute health impacts of O₃ are shown in **Table S4**. The
468 estimated annual all-cause premature deaths induced by O₃ increase from 55,876 in 1981 to 162,370 in 2019 with an
469 increasing trend of +2,979 deaths yr⁻¹. The annual premature deaths related to respiratory and cardiovascular diseases are
470 34,155 and 40,323 in 1998, and 26,471 and 79,021 in 2019, having a rate of change of -546 and +1,773 deaths yr⁻¹ during
471 1998–2019, respectively (**Fig. 10a**). Among three types of health outcomes, only respiratory diseases experienced a
472 decreasing trend in premature mortality, and the premature mortality is constantly below 40,000. The decreasing trend of
473 the respiration-related mortality primarily results from the decreased annual baseline mortality rate over the past decades
474 (**Fig. S12**). As the total respiratory-related deaths decreased over the past decades, respiratory O₃ deaths are decreasing
475 even under aggravated O₃ pollution. Based on GEOS-Chem-simulated O₃, the corresponding estimated change rate for all-
476 cause disease is +3,516 deaths yr⁻¹ from 50,384 in 1981 to 176,741 in 2019. Premature mortality induced by respiratory
477 disease decreases from 37,822 in 1998 to 29,079 in 2019 with a change rate of -584 deaths yr⁻¹, while cardiovascular
478 disease increases from 44,516 in 1998 to 85,980 in 2019 with a change rate of +1,977 deaths yr⁻¹ (**Fig. S13**). The result
479 shows that using GEOS-Chem-simulated O₃ generally gives higher estimates of mortality than using the bias-corrected
480 data. **Fig. 10b** shows the provincial annual average premature mortality of different health endpoints. The five provinces
481 with the highest all-cause mortality are Jiangsu [14,510 (95% CI: 9,022–19,935)], Shandong [12,684 (95% CI: 4,258–
482 20,990)], Henan [12,290 (95% CI: 4,125–20,343)], Guangdong [9,268 (95% CI: 7,224–11,416)] and Hebei [8,276 (95%
483 CI: 2,776–13,706)], which are generally consistent with previous studies for China (Zhang et al., 2021; Zhang et al., 2022a).
484 Similar distribution can be found for respiratory and cardiovascular diseases but with a different ranking order. Generally,
485 those provinces in densely populated areas (**Fig. 10c**) with higher O₃ concentrations, such as BTHs, YRD and PRD, have
486 higher health burdens. In contrast, the northeastern and southern China (excluding Guangdong) suffer the least life losses
487 induced by O₃ exposure (**Fig. S14**).

488 When compared with estimates from previous studies, our estimates of are generally quite consistent with that given
489 by Maji and Namdeo (2021), which reported that the short-term all-cause, cardiovascular and respiratory premature
490 mortalities attributed to ambient O₃ exposure were 156,000, 73,500 and 28,600 in 2019. Based on O₃ observations in 334
491 Chinese cities, Zhang et al. (2021) suggested that the national all-cause, respiratory, cardiovascular mortalities attributable
492 to O₃ are 270,000 to 390,000, 49,000 to 63,000, and 150,000 to 220,000 million across 2015–2018, which are much higher
493 than most existing results. Since the methodological approaches are largely similar and we use the log-linear exposure-
494 response function, we ascribe that the very high estimated mortalities are mainly due to concentration–response threshold
495 X_0 assumed to be zero in their study. A lower X_0 means that O₃ can cause more adverse impacts on human health even at
496 low concentrations, thus leading to higher mortalities.



497
 498 **Figure 10. (a) Annual premature mortality (thousand) for different diseases over the past decades; (b) annual mean**
 499 **province-based mortality (thousand) attributed to different health endpoints; and (c) annual mean province-based**
 500 **population (million). The mortality is calculated using the bias-corrected O₃.**

501 **4. Conclusions and discussion**

502 In this study, to have a more accurate characterization of O₃ spatiotemporal distribution and trends as well as their
 503 impacts on agriculture and human health, we used a hybrid approach to generate bias-corrected O₃ data across China from
 504 1981 to 2019. The hybrid approach helps improve O₃ predictions by taking advantage of a chemical transport model, a ML
 505 algorithm and increasing availability of high-resolution environmental and meteorological data. The validation shows that
 506 the bias-corrected O₃ can achieve a higher prediction accuracy than GEOS-Chem-simulated O₃ alone when compared with
 507 historical in-situ measurements. Before being corrected, the GEOS-Chem-simulated O₃ concentrations tend to be
 508 overestimated and lead to higher crop yield losses and larger O₃-induced mortalities. Noticeable differences in crop RYLs
 509 and mortality estimates highlight the advantages of using high-resolution O₃ data to improve our understanding of long-
 510 term O₃ impacts.

511 When examining the regional and national O₃ trends, we found that MDA8-O₃ concentrations have a perceptible
 512 increasing trend before 2000s, but fluctuate within a certain range with large interannual variabilities in more recent years.
 513 The large discrepancies in previous studies indicate that the regional and national O₃ trends in China still suffer with great
 514 uncertainties, particularly when different approaches are used to produce the O₃ estimates. However, these studies using
 515 source-varied O₃ fields consistently show the great interannual variabilities of O₃ concentrations. Some insights can be
 516 obtained from existing findings, which need to be carefully considered when examining O₃ trends and comparing them
 517 with existing results. First, given the large site differences, the calculation of observational O₃ trends is very sensitive to
 518 the subsets of data from networks. Thus, great uncertainty could still exist even using O₃ observations from the same source
 519 depending on the chosen subsets of data. Second, different formats of O₃ fields (e.g., site-based and gridded) could lead to



520 large uncertainties of the O₃ trend estimates. A higher resolution of gridded O₃ estimates from CTMs and ML may reduce
521 the differences between O₃ observational results. Third, the calculated O₃ trends are very sensitive to the chosen study
522 period due to large interannual variability and seasonal differences. The changing meteorological conditions are the major
523 factor causing the large interannual O₃ variations, and reductions in the emissions of NO_x, SO₂ and PM also have complex
524 effects on ground-level O₃ concentrations (Wang et al., 2022b). Liu and Wang (2020b) suggested that the meteorological
525 impacts on O₃ trends vary region by region and year by year and could be comparable with or even larger than the impacts
526 of changes in anthropogenic emissions.

527 Our estimated RYLs for maize and rice and soybean in China are generally consistent to existing studies, while the
528 RYLs for soybean and wheat are lower than their estimates mainly due to the differences in used metrics, O₃ fields and
529 crop sensitivity to ambient O₃ concentrations. It suggests that plating O₃-resistant cultivars could be an effective approach
530 to increase total crop production to meet the increasing food demands. In addition to the metrics and O₃ fields, uncertainties
531 of estimated O₃-induced crop losses could be also from other sources (e.g., dose-yield relationships). Though some other
532 metrics (e.g., M7/M12 and W126) have also been used in some studies (Van Dingenen et al., 2009; Avnery et al., 2013;
533 Wang et al., 2022c), there are not available dose-relationships for all four major crops specific for China. The estimated
534 RYLs for crops could be largely biased using metrics with dose-yield relationships developed for U.S. or Europe (**Fig.S15**),
535 as they are inadequate to represent Asian crop genotypes and environmental conditions. So, the region-specific dose-yield
536 relationships are highly recommended to be used in future study estimating the O₃-induced crop reduction, especially for
537 the regional study. Moreover, it is worth noting that as the concentration-based metrics do not account for how crop
538 physiological responses to the changing atmospheric environment, the associated dose-yield relationships which is
539 currently useful may not hold in the future (Tai et al., 2021). So, the flux-based metrics and the process-based crop model
540 are more recommended to be used for future O₃ risk assessments, wherein more crop- and region-specific experiments and
541 trials are needed to acquire appropriate metrics and dose-response functions and calibrate the process-based crop model.

542 In recent years, although existing studies have made efforts to quantify the O₃-related health impacts in China, only a
543 few focused on the nationwide acute O₃ health burden assessment, particularly for assessment over multiple decades (Maji
544 and Namdeo, 2021; Sahu et al., 2021; Zhang et al., 2021; Zhang et al., 2022a). There are some remaining issues to be
545 addressed regarding O₃ health impacts. For instance, the existence of a “safe” threshold of O₃ levels still remains debated.
546 A recent study reported that no consistent evidence was found for a threshold in the O₃-mortality concentration-response
547 relationship in seven cities of Jiangsu Province, China during 2013–2014 (Chen et al., 2017; Maji and Namdeo, 2021).
548 Given the importance of the threshold assumption in assessing health effects of air pollution, more studies are needed to
549 determine a most likely threshold for O₃-mortality association in the future. Moreover, the multiple temporal O₃ metrics
550 (e.g., 1-h maximum and daytime average O₃ concentrations) have also been proved to play an important role in the
551 variability of estimated health effects, even though standard ratios are used to convert among multiple metrics (Anderson
552 and Bell, 2010). In addition to the uncertainties from varying methodologies, interpretation of the O₃ epidemiological
553 impact is also constrained by the variability in geographical, seasonal, and demographic characteristics (Yin et al., 2017b).
554 Liu et al. (2013) suggested that associations between O₃ and mortality appeared to be more evident during the cool season
555 than in the warm season, and stronger in the oldest age group and among those with less education. The effect modification
556 by population susceptibility and the confounding effects of concomitant exposures (temperature, particulate matter, etc.)
557 should be further considered in future works.

558 A major limitation of our study lies in the uncertain predictions in regions where monitoring data are scarce (e.g., the
559 western half of China). The monitoring sites are sparsely distributed in those areas, which may fail to capture the accurate
560 association between O₃ concentrations and various predictors there, especially considering that the ML algorithm has likely
561 over-emphasized such relationships in the data-intensive eastern regions. Second, the land use data were prescribed in 2013
562 due to the limited availability of data, and this may neglect some major land use changes in China over the past decades.
563 Though the land use data were found by the ML algorithm to contribute little to the overall model, more detailed land use



564 data are expected to further increase model accuracy. In addition, though concentration-based metrics are easy to calculate
565 and ensured to be scientifically sound in some experiments (Fuhrer et al., 1997; Mills et al., 2007), they do not consider
566 the active responses of plant ecophysiology to ambient climatic and environmental changes and thus likely inadequate for
567 examining yield losses in a future climate and atmospheric environment. Thus, flux-based metrics are recommended in
568 future studies to better understand the long-term evolution of crop losses over China (Feng et al., 2012; Zhang et al., 2017;
569 Tai et al., 2021; Pleijel et al., 2022). Despite these limitations, our study represents important progress in evaluating the
570 long-term, multidecadal health burdens and agricultural losses resulting from O₃ pollution in China, which can provide
571 important references for governments and agencies when making related policies to meet the imperative environment,
572 health, and food security demands.

573

574 **Competing interests**

575 The contact author has declared that neither they nor their co-authors have any competing interests. At least one of the
576 (co-)authors is a member of the editorial board of Atmospheric Chemistry and Physics.

577 **Acknowledgements**

578 This work was supported by the National Natural Science Foundation of China (NSFC)/Research Grants Council (RGC)
579 Joint Research Scheme (reference #: N_CUHK440/20, 42061160479) awarded to A. P. K. Tai and Z. Feng.

580 **References**

- 581 Abdullah, S., Ismail, M., and Fong, S. Y.: Multiple Linear Regression (MLR) models for long term PM10 concentration
582 forecasting during different monsoon seasons, *Journal of Sustainability Science and Management*, 12, 60-69, 2017.
- 583 Anderson, G. B. and Bell, M. L.: Does one size fit all? The suitability of standard ozone exposure metric conversion ratios
584 and implications for epidemiology, *Journal of Exposure Science & Environmental Epidemiology*, 20, 2-11,
585 <https://doi.org/10.1038/jes.2008.69>, 2010.
- 586 Avnery, S., Mauzerall, D. L., and Fiore, A. M.: Increasing global agricultural production by reducing ozone damages via
587 methane emission controls and ozone-resistant cultivar selection, *Global Change Biology*, 19, 1285-1299,
588 <https://doi.org/10.1111/gcb.12118>, 2013.
- 589 Bey, I., Jacob, D. J., Yantosca, R. M., Logan, J. A., Field, B. D., Fiore, A. M., Li, Q., Liu, H. Y., Mickley, L. J., and Schultz,
590 M. G.: Global modeling of tropospheric chemistry with assimilated meteorology: Model description and evaluation,
591 *Journal of Geophysical Research: Atmospheres*, 106, 23073-23095, <https://doi.org/10.1029/2001JD000807>, 2001.
- 592 Bi, J., Knowland, K. E., Keller, C. A., and Liu, Y.: Combining Machine Learning and Numerical Simulation for High-
593 Resolution PM2.5 Concentration Forecast, *Environ Sci Technol*, 56, 1544-1556,
594 <https://doi.org/10.1021/acs.est.1c05578>, 2022.
- 595 Chen, K., Zhou, L., Chen, X., Bi, J., and Kinney, P. L.: Acute effect of ozone exposure on daily mortality in seven cities of
596 Jiangsu Province, China: No clear evidence for threshold, *Environmental Research*, 155, 235-241,
597 <https://doi.org/10.1016/j.envres.2017.02.009>, 2017.
- 598 Chen, T. and Guestrin, C.: XGBoost: A Scalable Tree Boosting System, *Proceedings of the 22nd ACM SIGKDD*
599 *International Conference on Knowledge Discovery and Data Mining*, San Francisco, California, USA,
600 <https://doi.org/10.1145/2939672.2939785>, 2016.
- 601 Clifton, O. E., Fiore, A. M., Massman, W. J., Baublitz, C. B., Coyle, M., Emberson, L., Fares, S., Farmer, D. K., Gentine,
602 P., Gerosa, G., Guenther, A. B., Helmig, D., Lombardozzi, D. L., Munger, J. W., Patton, E. G., Pusede, S. E., Schwede,
603 D. B., Silva, S. J., Sorgel, M., Steiner, A. L., and Tai, A. P. K.: Dry Deposition of Ozone over Land: Processes,
604 Measurement, and Modeling, *Rev Geophys*, 58, <https://doi.org/10.1029/2019RG000670>, 2020.



- 605 Dang, R., Liao, H., and Fu, Y.: Quantifying the anthropogenic and meteorological influences on summertime surface ozone
606 in China over 2012–2017, *Science of The Total Environment*, 754, 142394,
607 <https://doi.org/10.1016/j.scitotenv.2020.142394>, 2021.
- 608 Dedoussi, I. C., Eastham, S. D., Monier, E., and Barrett, S. R. H.: Premature mortality related to United States cross-state
609 air pollution, *Nature*, 578, 261–265, <https://doi.org/10.1038/s41586-020-1983-8>, 2020.
- 610 Di, Q., Rowland, S., Koutrakis, P., and Schwartz, J.: A hybrid model for spatially and temporally resolved ozone exposures
611 in the continental United States, *Journal of the Air & Waste Management Association*, 67, 39–52,
612 <https://doi.org/10.1080/10962247.2016.1200159>, 2017.
- 613 Ding, A., Wang, T., Zhao, M., Wang, T., and Li, Z.: Simulation of sea-land breezes and a discussion of their implications
614 on the transport of air pollution during a multi-day ozone episode in the Pearl River Delta of China, *Atmospheric
615 Environment*, 38, 6737–6750, <https://doi.org/10.1016/j.atmosenv.2004.09.017>, 2004.
- 616 Emberson, L. D., Büker, P., Ashmore, M. R., Mills, G., Jackson, L. S., Agrawal, M., Atikuzzaman, M. D., Cinderby, S.,
617 Engardt, M., Jamir, C., Kobayashi, K., Oanh, N. T. K., Quadir, Q. F., and Wahid, A.: A comparison of North American
618 and Asian exposure–response data for ozone effects on crop yields, *Atmospheric Environment*, 43, 1945–1953,
619 <https://doi.org/10.1016/j.atmosenv.2009.01.005>, 2009.
- 620 Feng, Z., Calatayud, V., Zhu, J., and Kobayashi, K.: Ozone exposure- and flux-based response relationships with
621 photosynthesis of winter wheat under fully open air condition, *Science of The Total Environment*, 619–620, 1538–
622 1544, <https://doi.org/10.1016/j.scitotenv.2017.10.089>, 2018.
- 623 Feng, Z., Tang, H., Uddling, J., Pleijel, H., Kobayashi, K., Zhu, J., Oue, H., and Guo, W.: A stomatal ozone flux–response
624 relationship to assess ozone-induced yield loss of winter wheat in subtropical China, *Environmental Pollution*, 164,
625 16–23, <https://doi.org/10.1016/j.envpol.2012.01.014>, 2012.
- 626 Feng, Z., De Marco, A., Anav, A., Gualtieri, M., Sicard, P., Tian, H., Fornasier, F., Tao, F., Guo, A., and Paoletti, E.:
627 Economic losses due to ozone impacts on human health, forest productivity and crop yield across China, *Environ Int*,
628 131, 104966, [10.1016/j.envint.2019.104966](https://doi.org/10.1016/j.envint.2019.104966), 2019.
- 629 Feng, Z., Xu, Y., Kobayashi, K., Dai, L., Zhang, T., Agathokleous, E., Calatayud, V., Paoletti, E., Mukherjee, A., Agrawal,
630 M., Park, R. J., Oak, Y. J., and Yue, X.: Ozone pollution threatens the production of major staple crops in East Asia,
631 *Nature Food*, 3, 47–56, <https://doi.org/10.1038/s43016-021-00422-6>, 2022.
- 632 Fu, Y. and Tai, A. P. K.: Impact of climate and land cover changes on tropospheric ozone air quality and public health in
633 East Asia between 1980 and 2010, *Atmos. Chem. Phys.*, 15, 10093–10106, <https://doi.org/10.5194/acp-15-10093-2015>,
634 2015.
- 635 Fuhrer, J., Skärby, L., and Ashmore, M. R.: Critical levels for ozone effects on vegetation in Europe, *Environmental
636 Pollution*, 97, 91–106, [https://doi.org/10.1016/S0269-7491\(97\)00067-5](https://doi.org/10.1016/S0269-7491(97)00067-5), 1997.
- 637 Fusco, A. C. and Logan, J. A.: Analysis of 1970–1995 trends in tropospheric ozone at Northern Hemisphere midlatitudes
638 with the GEOS-CHEM model, *Journal of Geophysical Research: Atmospheres*, 108,
639 <https://doi.org/10.1029/2002JD002742>, 2003.
- 640 Gong, C. and Liao, H.: A typical weather pattern for ozone pollution events in North China, *Atmos. Chem. Phys.*, 19,
641 13725–13740, <https://doi.org/10.5194/acp-19-13725-2019>, 2019.
- 642 Gong, C., Yue, X., Liao, H., and Ma, Y.: A humidity-based exposure index representing ozone damage effects on vegetation,
643 *Environmental Research Letters*, 16, <https://doi.org/10.1088/1748-9326/abecbb>, 2021.
- 644 Guenther, A. B., Jiang, X., Heald, C. L., Sakuayanontvittaya, T., Duhl, T., Emmons, L. K., and Wang, X.: The Model of
645 Emissions of Gases and Aerosols from Nature version 2.1 (MEGAN2.1): an extended and updated framework for
646 modeling biogenic emissions, *Geosci. Model Dev.*, 5, 1471–1492, <https://doi.org/10.5194/gmd-5-1471-2012>, 2012.
- 647 Han, H., Liu, J., Shu, L., Wang, T., and Yuan, H.: Local and synoptic meteorological influences on daily variability in
648 summertime surface ozone in eastern China, *Atmos. Chem. Phys.*, 20, 203–222, <https://doi.org/10.5194/acp-20-203->



- 649 2020, 2020.
- 650 He, J., Wang, Y., Hao, J., Shen, L., and Wang, L.: Variations of surface O₃ in August at a rural site near Shanghai: influences
651 from the West Pacific subtropical high and anthropogenic emissions, *Environmental Science and Pollution Research*,
652 19, 4016-4029, <https://doi.org/10.1007/s11356-012-0970-5>, 2012.
- 653 Hoesly, R. M., Smith, S. J., Feng, L., Klimont, Z., Janssens-Maenhout, G., Pitkanen, T., Seibert, J. J., Vu, L., Andres, R. J.,
654 Bolt, R. M., Bond, T. C., Dawidowski, L., Kholod, N., Kurokawa, J. I., Li, M., Liu, L., Lu, Z., Moura, M. C. P.,
655 O'Rourke, P. R., and Zhang, Q.: Historical (1750–2014) anthropogenic emissions of reactive gases and aerosols from
656 the Community Emissions Data System (CEDS), *Geosci. Model Dev.*, 11, 369-408, <https://doi.org/10.5194/gmd-11-369-2018>, 2018.
- 657
- 658 Hu, X., Belle, J. H., Meng, X., Wildani, A., Waller, L. A., Strickland, M. J., and Liu, Y.: Estimating PM_{2.5} Concentrations
659 in the Conterminous United States Using the Random Forest Approach, *Environ Sci Technol*, 51, 6936-6944,
660 <https://doi.org/10.1021/acs.est.7b01210>, 2017.
- 661 Irrgang, C., Boers, N., Sonnewald, M., Barnes, E. A., Kadow, C., Staneva, J., and Saynisch-Wagner, J.: Towards neural
662 Earth system modelling by integrating artificial intelligence in Earth system science, *Nature Machine Intelligence*, 3,
663 667-674, <https://doi.org/10.1038/s42256-021-00374-3>, 2021.
- 664 Ivatt, P. D. and Evans, M. J.: Improving the prediction of an atmospheric chemistry transport model using gradient-boosted
665 regression trees, *Atmos. Chem. Phys.*, 20, 8063-8082, <https://doi.org/10.5194/acp-20-8063-2020>, 2020.
- 666 Jacob, D. J. and Winner, D. A.: Effect of climate change on air quality, *Atmospheric Environment*, 43, 51-63,
667 <https://doi.org/10.1016/j.atmosenv.2008.09.051>, 2009.
- 668 Jiang, Y. C., Zhao, T. L., Liu, J., Xu, X. D., Tan, C. H., Cheng, X. H., Bi, X. Y., Gan, J. B., You, J. F., and Zhao, S. Z.: Why
669 does surface ozone peak before a typhoon landing in southeast China?, *Atmos. Chem. Phys.*, 15, 13331-13338,
670 <https://doi.org/10.5194/acp-15-13331-2015>, 2015.
- 671 Kawase, H., Nagashima, T., Sudo, K., and Nozawa, T.: Future changes in tropospheric ozone under Representative
672 Concentration Pathways (RCPs), *Geophysical Research Letters*, 38, <https://doi.org/10.1029/2010GL046402>, 2011.
- 673 Lelieveld, J., Evans, J. S., Fnais, M., Giannadaki, D., and Pozzer, A.: The contribution of outdoor air pollution sources to
674 premature mortality on a global scale, *Nature*, 525, 367-371, <https://doi.org/10.1038/nature15371>, 2015.
- 675 Li, K., Jacob, D. J., Shen, L., Lu, X., De Smedt, I., and Liao, H.: Increases in surface ozone pollution in China from 2013
676 to 2019: anthropogenic and meteorological influences, *Atmospheric Chemistry and Physics*, 20, 11423-11433,
677 <https://doi.org/10.5194/acp-20-11423-2020>, 2020.
- 678 Li, Y., Zhao, X., Deng, X., and Gao, J.: The impact of peripheral circulation characteristics of typhoon on sustained ozone
679 episodes over the Pearl River Delta region, China, *Atmos. Chem. Phys.*, 22, 3861-3873, <https://doi.org/10.5194/acp-22-3861-2022>, 2022.
- 680
- 681 Lin, J. T., Youn, D., Liang, X. Z., and Wuebbles, D. J.: Global model simulation of summertime U.S. ozone diurnal cycle
682 and its sensitivity to PBL mixing, spatial resolution, and emissions, *Atmospheric Environment*, 42, 8470-8483,
683 <https://doi.org/10.1016/j.atmosenv.2008.08.012>, 2008.
- 684 Liu, H., Liu, S., Xue, B., Lv, Z., Meng, Z., Yang, X., Xue, T., Yu, Q., and He, K.: Ground-level ozone pollution and its
685 health impacts in China, *Atmospheric Environment*, 173, 223-230, <https://doi.org/10.1016/j.atmosenv.2017.11.014>,
686 2018.
- 687 Liu, J., Wang, L., Li, M., Liao, Z., Sun, Y., Song, T., Gao, W., Wang, Y., Li, Y., Ji, D., Hu, B., Kerminen, V. M., Wang, Y.,
688 and Kulmala, M.: Quantifying the impact of synoptic circulation patterns on ozone variability in northern China from
689 April to October 2013–2017, *Atmos. Chem. Phys.*, 19, 14477-14492, <https://doi.org/10.5194/acp-19-14477-2019>,
690 2019.
- 691 Liu, R., Ma, Z., Liu, Y., Shao, Y., Zhao, W., and Bi, J.: Spatiotemporal distributions of surface ozone levels in China from
692 2005 to 2017: A machine learning approach, *Environ Int*, 142, 105823, <https://doi.org/10.1016/j.envint.2020.105823>,



- 693 2020.
- 694 Liu, T., Li, T. T., Zhang, Y. H., Xu, Y. J., Lao, X. Q., Rutherford, S., Chu, C., Luo, Y., Zhu, Q., Xu, X. J., Xie, H. Y., Liu,
695 Z. R., and Ma, W. J.: The short-term effect of ambient ozone on mortality is modified by temperature in Guangzhou,
696 China, *Atmospheric Environment*, 76, 59-67, <https://doi.org/10.1016/j.atmosenv.2012.07.011>, 2013.
- 697 Liu, Y. and Wang, T.: Worsening urban ozone pollution in China from 2013 to 2017 – Part 2: The effects of emission
698 changes and implications for multi-pollutant control, *Atmos. Chem. Phys.*, 20, 6323-6337,
699 <https://doi.org/10.5194/acp-20-6323-2020>, 2020a.
- 700 Liu, Y. and Wang, T.: Worsening urban ozone pollution in China from 2013 to 2017 – Part 1: The complex and varying
701 roles of meteorology, *Atmospheric Chemistry and Physics*, 20, 6305-6321, <https://doi.org/10.5194/acp-20-6305-2020>,
702 2020b.
- 703 Lu, C., Mao, J., Wang, L., Guan, Z., Zhao, G., and Li, M.: An unusual high ozone event over the North and Northeast China
704 during the record-breaking summer in 2018, *J Environ Sci (China)*, 104, 264-276,
705 <https://doi.org/10.1016/j.jes.2020.11.030>, 2021.
- 706 Lu, X., Hong, J., Zhang, L., Cooper, O. R., Schultz, M. G., Xu, X., Wang, T., Gao, M., Zhao, Y., and Zhang, Y.: Severe
707 Surface Ozone Pollution in China: A Global Perspective, *Environmental Science & Technology Letters*, 5, 487-494,
708 <https://doi.org/10.1021/acs.estlett.8b00366>, 2018.
- 709 Lu, X., Zhang, L., Chen, Y., Zhou, M., Zheng, B., Li, K., Liu, Y., Lin, J., Fu, T.-M., and Zhang, Q.: Exploring 2016–2017
710 surface ozone pollution over China: source contributions and meteorological influences, *Atmospheric Chemistry and
711 Physics*, 19, 8339-8361, <https://doi.org/10.5194/acp-19-8339-2019>, 2019.
- 712 Ma, R., Ban, J., Wang, Q., Zhang, Y., Yang, Y., He, M. Z., Li, S., Shi, W., and Li, T.: Random forest model based fine scale
713 spatiotemporal O₃ trends in the Beijing-Tianjin-Hebei region in China, 2010 to 2017, *Environ Pollut*, 276, 116635,
714 <https://doi.org/10.1016/j.envpol.2021.116635>, 2021.
- 715 Madaniyazi, L., Nagashima, T., Guo, Y., Pan, X., and Tong, S.: Projecting ozone-related mortality in East China,
716 *Environment International*, 92-93, 165-172, <https://doi.org/10.1016/j.envint.2016.03.040>, 2016.
- 717 Maji, K. J. and Namdeo, A.: Continuous increases of surface ozone and associated premature mortality growth in China
718 during 2015–2019, *Environmental Pollution*, 269, 116183, <https://doi.org/10.1016/j.envpol.2020.116183>, 2021.
- 719 Mao, J., Wang, L., Lu, C., Liu, J., Li, M., Tang, G., Ji, D., Zhang, N., and Wang, Y.: Meteorological mechanism for a large-
720 scale persistent severe ozone pollution event over eastern China in 2017, *J Environ Sci (China)*, 92, 187-199,
721 <https://doi.org/10.1016/j.jes.2020.02.019>, 2020.
- 722 Mills, G., Buse, A., Gimeno, B., Bermejo, V., Holland, M., Emberson, L., and Pleijel, H.: A synthesis of AOT40-based
723 response functions and critical levels of ozone for agricultural and horticultural crops, *Atmospheric Environment*, 41,
724 2630-2643, <https://doi.org/10.1016/j.atmosenv.2006.11.016>, 2007.
- 725 Mills, G., Sharps, K., Simpson, D., Pleijel, H., Frei, M., Burkey, K., Emberson, L., Uddling, J., Broberg, M., Feng, Z.,
726 Kobayashi, K., and Agrawal, M.: Closing the global ozone yield gap: Quantification and cobenefits for multistress
727 tolerance, *Global Change Biology*, 24, 4869-4893, <https://doi.org/10.1111/gcb.14381>, 2018.
- 728 Moustris, K. P., Nastos, P. T., Larissi, I. K., and Paliatsos, A. G.: Application of Multiple Linear Regression Models and
729 Artificial Neural Networks on the Surface Ozone Forecast in the Greater Athens Area, Greece, *Advances in
730 Meteorology*, 2012, 894714, <https://doi.org/10.1155/2012/894714>, 2012.
- 731 Mukherjee, A., Yadav, D. S., Agrawal, S. B., and Agrawal, M.: Ozone a persistent challenge to food security in India:
732 Current status and policy implications, *Current Opinion in Environmental Science & Health*, 19, 100220,
733 <https://doi.org/10.1016/j.coesh.2020.10.008>, 2021.
- 734 Pleijel, H., Danielsson, H., and Broberg, M. C.: Benefits of the Phytotoxic Ozone Dose (POD) index in dose-response
735 functions for wheat yield loss, *Atmospheric Environment*, 268, 118797,
736 <https://doi.org/10.1016/j.atmosenv.2021.118797>, 2022.



- 737 Sacks, W. J., Deryng, D., Foley, J. A., and Ramankutty, N.: Crop planting dates: an analysis of global patterns, *Global*
738 *Ecology and Biogeography*, 19, 607-620, <https://doi.org/10.1111/j.1466-8238.2010.00551.x>, 2010.
- 739 Sahu, S. K., Liu, S., Liu, S., Ding, D., and Xing, J.: Ozone pollution in China: Background and transboundary contributions
740 to ozone concentration & related health effects across the country, *Sci Total Environ*, 761, 144131,
741 <https://doi.org/10.1016/j.scitotenv.2020.144131>, 2021.
- 742 Shang, Y., Sun, Z., Cao, J., Wang, X., Zhong, L., Bi, X., Li, H., Liu, W., Zhu, T., and Huang, W.: Systematic review of
743 Chinese studies of short-term exposure to air pollution and daily mortality, *Environment International*, 54, 100-111,
744 <https://doi.org/10.1016/j.envint.2013.01.010>, 2013.
- 745 Sindelarova, K., Granier, C., Bouarar, I., Guenther, A., Tilmes, S., Stavrou, T., Müller, J. F., Kuhn, U., Stefani, P., and
746 Knorr, W.: Global data set of biogenic VOC emissions calculated by the MEGAN model over the last 30 years, *Atmos.*
747 *Chem. Phys.*, 14, 9317-9341, <https://doi.org/10.5194/acp-14-9317-2014>, 2014.
- 748 Tai, A. P. K., Mickley, L. J., Heald, C. L., and Wu, S.: Effect of CO₂ inhibition on biogenic isoprene emission: Implications
749 for air quality under 2000 to 2050 changes in climate, vegetation, and land use, *Geophysical Research Letters*, 40,
750 3479-3483, <https://doi.org/10.1002/grl.50650>, 2013.
- 751 Tai, A. P. K., Sadiq, M., Pang, J. Y. S., Yung, D. H. Y., and Feng, Z.: Impacts of Surface Ozone Pollution on Global Crop
752 Yields: Comparing Different Ozone Exposure Metrics and Incorporating Co-effects of CO₂, *Frontiers in Sustainable*
753 *Food Systems*, 5, <https://doi.org/10.3389/fsufs.2021.534616>, 2021.
- 754 Travis, K. R., Jacob, D. J., Fisher, J. A., Kim, P. S., Marais, E. A., Zhu, L., Yu, K., Miller, C. C., Yantosca, R. M., Sulprizio,
755 M. P., Thompson, A. M., Wennberg, P. O., Crouse, J. D., St. Clair, J. M., Cohen, R. C., Laughner, J. L., Dibb, J. E.,
756 Hall, S. R., Ullmann, K., Wolfe, G. M., Pollack, I. B., Peischl, J., Neuman, J. A., and Zhou, X.: Why do models
757 overestimate surface ozone in the Southeast United States?, *Atmos. Chem. Phys.*, 16, 13561-13577,
758 <https://doi.org/10.5194/acp-16-13561-2016>, 2016.
- 759 van der Werf, G. R., Randerson, J. T., Giglio, L., van Leeuwen, T. T., Chen, Y., Rogers, B. M., Mu, M., van Marle, M. J.
760 E., Morton, D. C., Collatz, G. J., Yokelson, R. J., and Kasibhatla, P. S.: Global fire emissions estimates during 1997–
761 2016, *Earth Syst. Sci. Data*, 9, 697-720, <https://doi.org/10.5194/essd-9-697-2017>, 2017.
- 762 Van Dingenen, R., Dentener, F. J., Raes, F., Krol, M. C., Emberson, L., and Cofala, J.: The global impact of ozone on
763 agricultural crop yields under current and future air quality legislation, *Atmospheric Environment*, 43, 604-618,
764 <https://doi.org/10.1016/j.atmosenv.2008.10.033>, 2009.
- 765 Wang, H., Lyu, X., Guo, H., Wang, Y., Zou, S., Ling, Z., Wang, X., Jiang, F., Zeren, Y., Pan, W., Huang, X., and Shen, J.:
766 Ozone pollution around a coastal region of South China Sea: interaction between marine and continental air, *Atmos.*
767 *Chem. Phys.*, 18, 4277-4295, <https://doi.org/10.5194/acp-18-4277-2018>, 2018.
- 768 Wang, H., Lu, X., Jacob, D. J., Cooper, O. R., Chang, K. L., Li, K., Gao, M., Liu, Y., Sheng, B., Wu, K., Wu, T., Zhang, J.,
769 Sauvage, B., Nédélec, P., Blot, R., and Fan, S.: Global tropospheric ozone trends, attributions, and radiative impacts
770 in 1995–2017: an integrated analysis using aircraft (IAGOS) observations, ozonesonde, and multi-decadal chemical
771 model simulations, *Atmos. Chem. Phys.*, 22, 13753-13782, <https://doi.org/10.5194/acp-22-13753-2022>, 2022a.
- 772 Wang, L., Tai, A. P. K., Tam, C.-Y., Sadiq, M., Wang, P., and Cheung, K. K. W.: Impacts of future land use and land cover
773 change on mid-21st-century surface ozone air quality: distinguishing between the biogeophysical and biogeochemical
774 effects, *Atmospheric Chemistry and Physics*, 20, 11349-11369, <https://doi.org/10.5194/acp-20-11349-2020>, 2020.
- 775 Wang, T., Xue, L., Feng, Z., Dai, J., Zhang, Y., and Tan, Y.: Ground-level ozone pollution in China: a synthesis of recent
776 findings on influencing factors and impacts, *Environmental Research Letters*, 17, 063003,
777 <https://doi.org/10.1088/1748-9326/ac69fe>, 2022b.
- 778 Wang, X., Gong, G., Li, N., and Qiu, S.: Detection Analysis of Epileptic EEG Using a Novel Random Forest Model
779 Combined With Grid Search Optimization, *Frontiers in Human Neuroscience*, 13,
780 <https://doi.org/10.3389/fnhum.2019.00052>, 2019.



- 781 Wang, Y., Zhang, Y., Hao, J., and Luo, M.: Seasonal and spatial variability of surface ozone over China: contributions from
782 background and domestic pollution, *Atmos. Chem. Phys.*, 11, 3511-3525, <https://doi.org/10.5194/acp-11-3511-2011>,
783 2011.
- 784 Wang, Y., Shen, L., Wu, S., Mickley, L., He, J., and Hao, J.: Sensitivity of surface ozone over China to 2000–2050 global
785 changes of climate and emissions, *Atmospheric Environment*, 75, 374-382,
786 <https://doi.org/10.1016/j.atmosenv.2013.04.045>, 2013.
- 787 Wang, Y., Wild, O., Ashworth, K., Chen, X., Wu, Q., Qi, Y., and Wang, Z.: Reductions in crop yields across China from
788 elevated ozone, *Environmental Pollution*, 292, 118218, <https://doi.org/10.1016/j.envpol.2021.118218>, 2022c.
- 789 Wei, J., Li, Z., Li, K., Dickerson, R. R., Pinker, R. T., Wang, J., Liu, X., Sun, L., Xue, W., and Cribb, M.: Full-coverage
790 mapping and spatiotemporal variations of ground-level ozone (O₃) pollution from 2013 to 2020 across China, *Remote
791 Sensing of Environment*, 270, 112775, <https://doi.org/10.1016/j.rse.2021.112775>, 2022.
- 792 Wesely, M. L.: Parameterization of surface resistances to gaseous dry deposition in regional-scale numerical models,
793 *Atmospheric Environment* (1967), 23, 1293-1304, [https://doi.org/10.1016/0004-6981\(89\)90153-4](https://doi.org/10.1016/0004-6981(89)90153-4), 1989.
- 794 Xiao, Q., Chang, H. H., Geng, G., and Liu, Y.: An Ensemble Machine-Learning Model To Predict Historical PM_{2.5}
795 Concentrations in China from Satellite Data, *Environmental Science & Technology*, 52, 13260-13269,
796 <https://doi.org/10.1021/acs.est.8b02917>, 2018.
- 797 Yang, L., Luo, H., Yuan, Z., Zheng, J., Huang, Z., Li, C., Lin, X., Louie, P. K. K., Chen, D., and Bian, Y.: Quantitative
798 impacts of meteorology and precursor emission changes on the long-term trend of ambient ozone over the Pearl River
799 Delta, China, and implications for ozone control strategy, *Atmos. Chem. Phys.*, 19, 12901-12916,
800 <https://doi.org/10.5194/acp-19-12901-2019>, 2019.
- 801 Yin, H., Pizzol, M., and Xu, L.: External costs of PM_{2.5} pollution in Beijing, China: Uncertainty analysis of multiple health
802 impacts and costs, *Environ Pollut*, 226, 356-369, <https://doi.org/10.1016/j.envpol.2017.02.029>, 2017a.
- 803 Yin, P., Chen, R., Wang, L., Meng, X., Liu, C., Niu, Y., Lin, Z., Liu, Y., Liu, J., Qi, J., You, J., Zhou, M., and Kan, H.:
804 Ambient Ozone Pollution and Daily Mortality: A Nationwide Study in 272 Chinese Cities, *Environ Health Perspect*,
805 125, 117006, <https://doi.org/10.1289/EHP1849>, 2017b.
- 806 Yin, Z. and Ma, X.: Meteorological conditions contributed to changes in dominant patterns of summer ozone pollution in
807 Eastern China, *Environmental Research Letters*, 15, <https://doi.org/10.1088/1748-9326/abc915>, 2020.
- 808 Zhan, Y., Luo, Y., Deng, X., Chen, H., Grieneisen, M. L., Shen, X., Zhu, L., and Zhang, M.: Spatiotemporal prediction of
809 continuous daily PM_{2.5} concentrations across China using a spatially explicit machine learning algorithm,
810 *Atmospheric Environment*, 155, 129-139, <https://doi.org/10.1016/j.atmosenv.2017.02.023>, 2017.
- 811 Zhang, W., Feng, Z., Wang, X., Liu, X., and Hu, E.: Quantification of ozone exposure- and stomatal uptake-yield response
812 relationships for soybean in Northeast China, *Science of The Total Environment*, 599-600, 710-720,
813 <https://doi.org/10.1016/j.scitotenv.2017.04.231>, 2017.
- 814 Zhang, X., Osei, F., Stein, A., Cheng, C., and Maji, K. J.: Temporal and spatial evolution of short-term exposure to ozone
815 pollution: Its health impacts in China based on a meta-analysis, *Journal of Cleaner Production*, 373, 133938,
816 <https://doi.org/10.1016/j.jclepro.2022.133938>, 2022a.
- 817 Zhang, X., Yan, B., Zhou, Y., Osei, F., Li, Y., Zhao, H., Cheng, C., and Stein, A.: Short-term health impacts related to ozone
818 in China before and after implementation of policy measures: A systematic review and meta-analysis, *Science of The
819 Total Environment*, 847, 157588, <https://doi.org/10.1016/j.scitotenv.2022.157588>, 2022b.
- 820 Zhang, Y., Wang, Y., Gao, M., Ma, Q., Zhao, J., Zhang, R., Wang, Q., and Huang, L.: A Predictive Data Feature Exploration-
821 Based Air Quality Prediction Approach, *IEEE Access*, 7, 30732-30743,
822 <https://doi.org/10.1109/ACCESS.2019.2897754>, 2019.
- 823 Zhang, Z., Yao, M., Wu, W., Zhao, X., and Zhang, J.: Spatiotemporal assessment of health burden and economic losses
824 attributable to short-term exposure to ground-level ozone during 2015-2018 in China, *BMC Public Health*, 21, 1069,



825 <https://doi.org/10.1186/s12889-021-10751-7>, 2021.
826 Zhao, Z. and Wang, Y.: Influence of the West Pacific subtropical high on surface ozone daily variability in summertime
827 over eastern China, *Atmospheric Environment*, 170, 197-204, <https://doi.org/10.1016/j.atmosenv.2017.09.024>, 2017.
828 Zhou, D., Ding, A., Mao, H., Fu, C., Wang, T., Chan, L. Y., Ding, K., Zhang, Y., Liu, J., Lu, A., and Hao, N.: Impacts of
829 the East Asian monsoon on lower tropospheric ozone over coastal South China, *Environmental Research Letters*, 8,
830 044011, <https://doi.org/10.1088/1748-9326/8/4/044011>, 2013.
831